The Green Bank Ammonia Survey: Dense Cores under Pressure in Orion A

Draft version August 21, 2017
Typeset using LaTeX **preprint** style in AASTeX61

THE GREEN BANK AMMONIA SURVEY: DENSE CORES UNDER PRESSURE IN ORION A

Helen Kirk,[1] Rachel K. Friesen,[2] Jaime E. Pineda,[3] Erik Rosolowsky,[4] Stella S. R. Offner,[5] Christopher D. Matzner,[6] Philip C. Myers,[7] James Di Francesco,[1,8] Paola Caselli,[3] Felipe O. Alves,[3] Ana Chacón-Tanarro,[3] How-Huan Chen,[7] Michael Chun-Yuan Chen,[8] Jared Keown,[8] Anna Punanova,[3] Young Min Seo,[9] Yancy Shirley,[10] Adam Ginsburg,[11] Christine Hall,[12] Ayushi Singh,[6] Héctor G. Arce,[13] Alyssa A. Goodman,[7] Peter Martin,[14] and Elena Redaelli[3]

[1]*NRC Herzberg Astronomy and Astrophysics, 5071 West Saanich Rd, Victoria, BC, V9E 2E7, Canada*
[2]*Dunlap Institute for Astronomy & Astrophysics, University of Toronto, 50 St. George Street, Toronto, Ontario, Canada M5S 3H4*
[3]*Max-Planck-Institut für extraterrestrische Physik, Giessenbachstrasse 1, D-85748, Garching, Germany*
[4]*Department of Physics, University of Alberta, Edmonton, AB, Canada*
[5]*Department of Astronomy, University of Massachusetts, Amherst, MA 01003, USA*
[6]*Department of Astronomy & Astrophysics, University of Toronto, 50 St. George Street, Toronto, Ontario, Canada M5S 3H4*
[7]*Harvard-Smithsonian Center for Astrophysics, 60 Garden St., Cambridge, MA 02138, USA*
[8]*Department of Physics and Astronomy, University of Victoria, 3800 Finnerty Road, Victoria, BC, Canada V8P 5C2*
[9]*Jet Propulsion Laboratory, NASA, 4800 Oak Grove Dr, Pasadena, CA 91109, USA*
[10]*Steward Observatory, 933 North Cherry Avenue, Tucson, AZ 85721, USA*
[11]*National Radio Astronomy Observatory, Socorro, NM 87801, USA*
[12]*Department of Physics, Engineering Physics & Astronomy, Queen's University, Kingston, Ontario, Canada K7L 3N6*
[13]*Department of Astronomy, Yale University, P.O. Box 208101, New Haven, CT 06520-8101, USA*
[14]*Canadian Institute for Theoretical Astrophysics, University of Toronto, 60 St. George St., Toronto, Ontario, Canada, M5S 3H8*

ABSTRACT

We use gas temperature and velocity dispersion data from the Green Bank Ammonia Survey and core masses and sizes from the James Clerk Maxwell Telescope Gould Belt Survey to estimate the virial states of dense cores within the Orion A molecular cloud. Surprisingly, we find that almost none of the dense cores are sufficiently massive to be bound when considering only the balance between self-gravity and the thermal and non-thermal motions present in the dense gas. Including the additional pressure binding imposed by the weight of the ambient molecular cloud material and additional smaller pressure terms, however, suggests that most of the dense cores are pressure confined.

1. INTRODUCTION

Dense cores, ∼0.1 pc-sized condensations of gas and dust, are the birthplaces of stars (e.g., Bergin & Tafalla 2007; Di Francesco et al. 2007; Ward-Thompson et al. 2007a). One of the most important properties of a dense core is its degree of stability against gravitational collapse. Understanding which subset of cores in a molecular cloud population is likely to form protostars in the near future, versus which subset of cores is likely to not form protostars soon (or ever, unless local conditions change) has profound implications for star formation efficiency and the interpretation of the core mass function. Detailed studies of individual cores (including full 3-D modelling, e.g., Steinacker et al. 2013) are essential for accurately determining all properties of an individual system. This approach, however, requires a prohibitive amount of data and modelling time for cloud-wide core population studies. Instead, by adopting simple stability proxies, insight can be gained into the global properties and variations of cores within a molecular cloud. Even this approach requires a non-negligible amount of information, including mass, temperature, non-thermal motions, and other properties that are typically estimated from different types of observations. The Green Bank Ammonia Survey (GAS; Friesen & Pineda et al. 2017) provides an important contribution to these studies. Using the *Herschel* and JCMT Gould Belt Surveys (André et al. 2010; Ward-Thompson et al. 2007b) to identify high extinction areas within nearby molecular clouds (< 500 pc) that likely have dense gas, GAS data provide gas temperature and velocity information to complement the (dust) column density information collected by the Gould Belt Surveys. The large and uniform areal coverage of these three surveys provides an unprecedented opportunity to understand the broad stability properties of dense structures formed within nearby molecular clouds.

The Orion A molecular cloud is one of the most distant clouds covered by GAS and is located at a distance of ~ 415 pc from the Sun (Menten et al. 2007; Kim et al. 2008). Orion A is also the closest example of a molecular cloud forming high-mass stars. For example, there are several O stars forming within the Orion Nebula Cluster (e.g., Hillenbrand 1997; Bally 2008). The Orion A complex also hosts hundreds of mostly lower mass protostars (e.g., Megeath et al. 2012; Stutz et al. 2013) and many dense cores forming, or with the potential to form, additional protostars (e.g., Mezger et al. 1990; Johnstone & Bally 1999; Ikeda et al. 2007; Li et al. 2007; Sadavoy et al. 2010; Shimajiri et al. 2011; Polychroni et al. 2013; Salji et al. 2015; Mairs et al. 2016; Lane et al. 2016). The large census of dense cores, and extensive observations available for the region, in combination with its status as the nearest higher-mass star-forming region, make Orion A an ideal cloud in which to investigate core properties and boundedness.

The dense cores within the OMC2 and OMC3 regions of Orion A (i.e., the top portion of the Integral Shaped Filament) have previously been analyzed from a virial perspective by Li et al. (2013), using a combination of SCUBA data from Nutter & Ward-Thompson (2007) to identify the dense cores and NH_3 data from the VLA and GBT to estimate the velocity dispersion and kinetic temperature. While the spatial resolution of the NH_3 data is quite good, $5''$, the spectral resolution is poor, with a FWHM of 0.6 km s^{-1}, and Li et al. (2013) find that many of the dense cores have intrinsic line widths below their resolution.

Given the better velocity resolution and larger spatial coverage of our GAS observations, it is worth re-visiting a virial analysis of Orion A. Here, we combine data from the JCMT Gould Belt Survey, which identified dense cores and characterized their basic properties (size and mass) with

new dynamical data from GAS which trace the motions of the dense gas (NH_3) associated with these dense cores.

In Section 2, we present the GAS and JCMT GBS observations used in our analysis, along with supplementary publicly available data (e.g., protostellar catalogues and total cloud column density maps). In Section 3, we first perform a simple virial analysis comparing only self-gravity with thermal and non-thermal support, and find that most of the dense cores appear unbound under these assumptions. We then include confining pressure terms in our analysis and show that most of the cores are actually bound. In Section 4, we discuss our results in the context of external pressure binding being an important ingredient in all nearby star-forming regions, before concluding in Section 5.

2. OBSERVATIONS

2.1. *GBT NH_3 Observations*

NH_3 observations were obtained through the Green Bank Ammonia Survey (GAS), a large project to map the ammonia (1,1), (2,2), and (3,3) rotation-inversion transitions across the high-extinction regions of nearby Gould Belt molecular clouds using the Green Bank Telescope's K-band Focal Plane Array (KFPA). The survey strategy, data reduction procedure, and basic data properties are described in detail in Friesen & Pineda et al. (2017). The spatial resolution is 32″ (0.064 pc), while the spectral resolution is 0.07 km s^{-1}. Observations of the northern portion of the Orion A cloud are one of the first four areas mapped and are presented in Friesen & Pineda et al. (2017) as 'Data Release 1' (DR1)[1]. The DR1 observations of Orion A cover the integral shaped filament (ISF) and areas slightly southward of it. Additional data further south were obtained at a later date and will be included in a second data release. Figure 1 shows an overview of the area mapped overlaid on the JCMT SCUBA-2 850 μm image of the region, with the dense cores (see Section 2.2) and protostars (see Section 2.3) overlaid in each panel.

2.2. *JCMT SCUBA-2 data*

Although NH_3 is an excellent tracer of dense gas, defining dense cores from its emission alone can be complicated by varying abundance levels. At the distance of Orion ($\sim$ 415 pc; Menten et al. 2007; Kim et al. 2008), the $\sim$32″ resolution of our GAS data also presents a challenge in identifying individual dense cores in such a complex and clustered environment. Submillimetre continuum emission offers an alternative method to identifying dense cores and estimating their sizes and masses. There are, however several separate significant sources of uncertainty in the conversion between flux density and mass, as well as the potential for chance alignments of lower density structures giving rise to apparent cores. The James Clerk Maxwell Telescope Gould Belt Survey (JCMT GBS; Ward-Thompson et al. 2007b) observed 6.2 square degrees around the Orion A molecular cloud at 850 μm and 450 μm with SCUBA-2, with resolutions of 14.6″ and 9.8″ (Dempsey et al. 2013), respectively. Observations of the northern and southern portions of Orion A were first published in Salji et al. (2015) and Mairs et al. (2016), respectively. For our analysis, we use the dense core catalogue presented in Lane et al. (2016), which covers the entire Orion A complex.

Lane et al. (2016) analyzed the JCMT GBS 850 μm data for the entire Orion A molecular cloud, using a map which reaches the full survey depth but is slightly poorer at recovering the largest-scale

[1] DR1 maps and data products are all publicly available at `https://dataverse.harvard.edu/dataverse/GAS_DR1`.

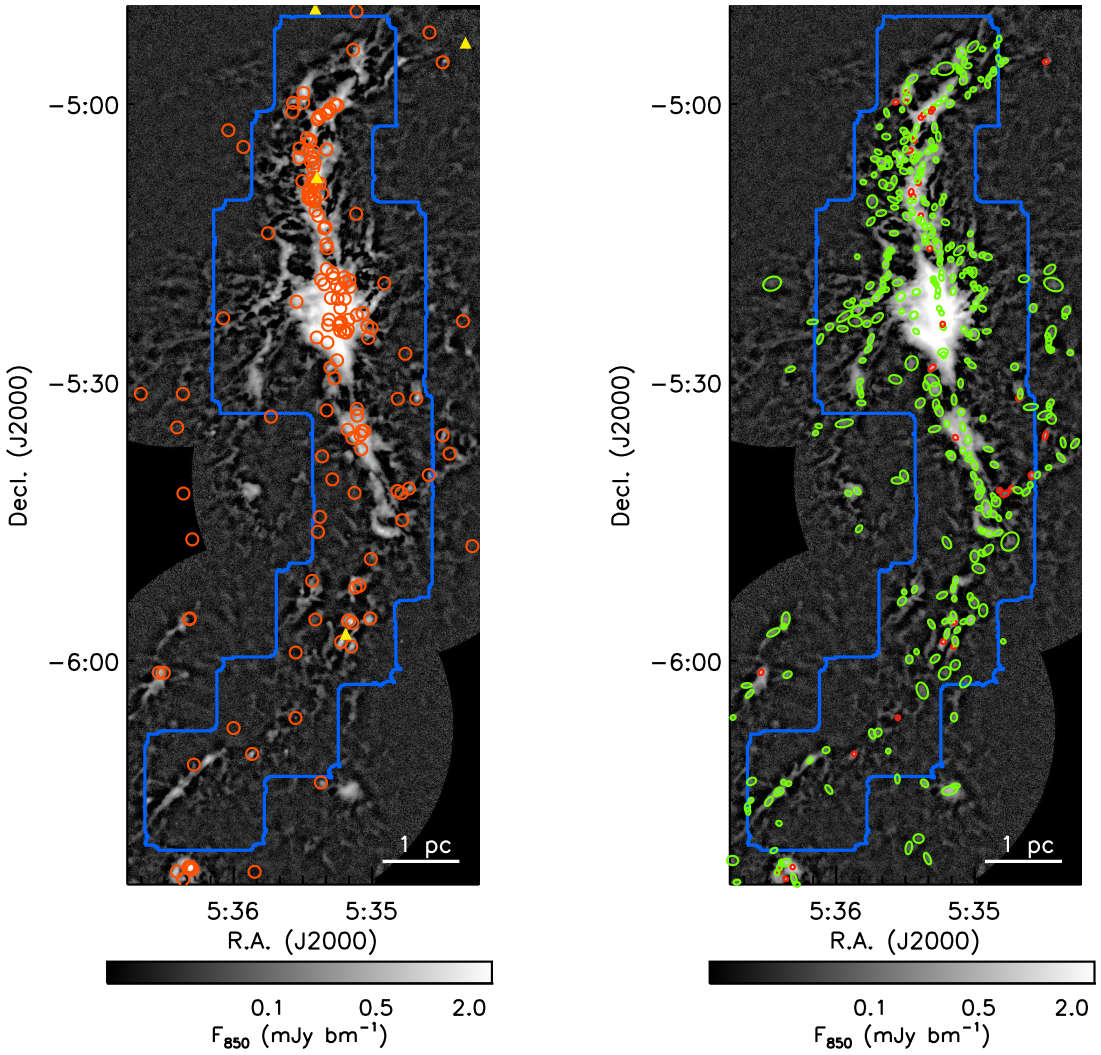

Figure 1. An overview of the JCMT GBS 850 μm data over the portion of Orion A observed by GAS. The blue contour shows the areal coverage of GAS for the present DR1 analysis. In the left panel, the dark orange circles show YSOs identified using *Spitzer* data (Megeath et al. 2012), while the filled yellow triangles show additional YSOs identified using *Herschel* data (Stutz et al. 2013). In the right panel, the ellipses show the Gaussian 1-sigma contours fit to the culled *getsources* core catalogue of Lane et al. (2016). Here, protostellar cores are shown in red while starless cores are shown in green.

structures than the current best reduction method. Lane et al. (2016) identified dense cores using two independent methods, *getsources* (Men'shchikov et al. 2012) and *FellWalker* (Berry 2015), and analyzed their clustering properties. The *getsources* algorithm is a multi-scale, multi-wavelength source extraction algorithm. *Getsources* first decomposes emission from each wavelength into a variety of scales, and then uses the combined information across wavelengths to create a Gaussian-based model that characterizes the small-scale sources and separates them from larger-scale emission features. In contrast, the *FellWalker* algorithm separates peaks based on local gradients, assigning each pixel to the peak that the local gradient points towards. *FellWalker* therefore does not assume any particular source geometry and in the Lane et al. (2016) catalogue, no background subtraction

was performed to remove large-scale structures. Since Orion A is home to quite complex emission structures, Lane et al. (2016) found that in general *getsources* performed better in isolating dense and compact structures. For our main analysis, we therefore adopt the *getsources*-based catalogue of Lane et al. (2016), although in Appendix A, we present an analysis using instead the *FellWalker*-based catalogue. In Appendix A, we demonstrate that our results are robust against changes in the core catalogue used.

The Lane et al. (2016) Orion A catalogue provides the sizes, total fluxes, and peak positions of the dense cores. We approximate the dense core radius as the geometric mean of the major and minor axis FWHMs fit by *getsources*, noting that at a radius equal to the FWHM, a Gaussian profile is at one eighth of its full height, and is therefore a reasonable estimate of the full core extent. We assume a distance of 415 pc to Orion A, and correct the Lane et al. (2016) catalogue values from their assumed distance of 450 pc. We also correct the core sizes for the telescope beam; for cores with sizes less than half of the 14.6″ SCUBA-2 850 μm beam FWHM, deconvolution is likely to be unreliable, and so we report this value as the upper limit to their true size. We convert the total flux of each core measured by *getsources* to a mass using

$$M = 1.30\Big(\frac{S_{850}}{1\ \mathrm{Jy}}\Big)\Big(\frac{\kappa_{850}}{0.012\ \mathrm{cm^2\ g^{-1}}}\Big)\Big(exp\Big(\frac{17\ \mathrm{K}}{T_d}\Big)-1\Big)\Big(\frac{D}{450\ \mathrm{pc}}\Big)^2 M_\odot \quad (1)$$

where S_{850} is the total flux density at 850 μm, κ_{850} is the dust opacity at 850 μm, T_d is the dust temperature, and D is the distance. We assume a constant dust grain opacity at 850 μm of 0.012 cm^2 g^{-1}, consistent with previous JCMT and *Herschel* Gould Belt analyses, and which includes the standard dust to gas ratio of 0.01 (e.g., Kirk et al. 2013; Pattle et al. 2015). (Note that the popular Ossenkopf & Henning (1994) model 5 for icy grains would give a larger opacity of 0.018 cm^2 g^{-1} at 850 μm.) For each core, we adopt a dust temperature equal to the kinetic temperature derived from our GAS NH_3 observations (see Section 2.4). For cores where a kinetic temperature was not able to be measured, we assume a value of 18 K, which is the mean temperature measured for the cores in NH_3. Previous works, including Lane et al. (2016), assumed a constant dust temperature of 15 K, which would give masses roughly 30% larger than those quoted here for a mean dust temperature of 18 K. Similarly, assuming instead a higher temperature of 21 K would give masses that were 20% smaller. We note that while a 20% to 30% change in estimated mass can be significant for a detailed study of a single object, this level of difference has relatively little impact on our population study due to the broad range in properties measured. For example, most of the cores would not change their status of being gravitationally bound or unbound in Section 3.2 with only a 20% to 30% change in their mass. Much larger variations in the mass estimated for cores arise in regions of complex emission structure such as Orion A through the choice in algorithm used to identify cores. In Appendix A, the cores identified using *FellWalker* tend to be more massive with larger sizes than the *getsources* cores. Highlighting the challenges of core identification, there is not always a one-to-one correspondence between objects in the two catalogues, as *getsources* tends to split emission structures more finely than *FellWalker* does. Despite these large uncertainties in defining individual cores and accurately measuring their properties, our overall conclusions about the typical virial state of cores is similar using either algorithm, suggesting that our overall conclusions about bulk virial properties are robust.

Finally, we note that some of the dense cores in Lane et al. (2016), although they are clearly detected, have poor Gaussian fits. While this was not important for the original clustering analysis

of Lane et al. (2016), poor estimates of the core radius could significantly impact our virial analysis. We therefore apply several cuts to the Lane et al. (2016) *getsources* catalogue, requiring dense cores in our present analysis to have parameters:

`gs_sig_glob` $\geq$1
`gs_sig_mono8` $\geq$7
`gs_good` $>$ 0
`gs_relp850` $>$ 3
`gs_relt850` $>$ 3

In short, these criteria imply 'significant' fits (`gs_sig_glob, gs_sig_mono8`) with fitted peak fluxes of S/N $\geq$ 3 (`gs_relp850`) and fitted total fluxes of S/N $\geq$ 3 (`gs_relt850`), and no *getsources* flags (`gs_good`) associated with the fits. These fitting criteria reduce the original 919 dense cores in Lane et al. (2016) to 610, primarily excluding the faintest cores with the poorest fits. In the culled catalogue, the lowest mass core identified is 0.09 $M_\odot$. Of the 610 reliably fit dense cores, roughly half (311) lie within the area mapped by GAS. The median mass of the cores is 0.7 $M_\odot$ for those with reliable *getsources* sizes and reliable temperature and kinematic measures (see Section 2.4).

Figure 1 shows the GBS 850 μm emission over the area observed with GAS, with the culled *getsources* catalogue overlaid. The dearth of *getsources* cores in the centre of the ISF visible in Figure 1 is caused by two effects. First, *getsources* excludes large-scale emission modes from its core-fitting routine, and hence a significant amount of flux within the centre of the ISF is not attributed to any *getsources* core. Second, the larger-scale emission within the centre of the ISF increases the difficulty of fitting Gaussian models to the compact emission features present, leading to a greater fraction of cores being culled in this particular area. We note, however, that our overall results are similar even when the full *getsources* catalogue from Lane et al. (2016) is used.

In Table 1, we summarize the properties of the cores identified by *getsources* for which there are measurements of their GAS-derived properties (see following sections).

2.3. *Protostars*

Lane et al. (2016) further classify their dense cores as being protostellar or starless based on whether or not they are spatially coincident with a protostar identified by Megeath et al. (2012) using *Spitzer* observations or Stutz et al. (2013) using *Herschel* data. Due to the highly clustered nature of Orion A, Lane et al. (2016) required a separation of less than one beam radius (7.25″) from the dense core's peak location for a core to be classified as protostellar. Note that this small separation requirement ensures that any given protostar can be associated with a maximum of one dense core. Meingast et al. (2016) recently identified YSOs in Orion based on near infrared observations using VISTA. We searched their catalogue for evidence of additional protostellar cores, but found only three possible new associations with our core catalogue, all of which were listed in Meingast et al. (2016) as previously known class II sources. For simplicity, we did not re-classify these three cores. Protostellar and starless dense cores are shown in Figure 1 in the right-hand panel, while the protostars themselves are shown in the left-hand panel.

2.4. *Deriving Dynamical Core Properties*

The GAS NH_3 (1,1) and (2,2) observations were used to estimate the dense gas properties, as described in more detail in Friesen & Pineda et al. (2017). Our interest here is in the velocity dispersion, σ, and the kinetic temperature, T_{kin}. Figure 2 shows a comparison of T_{kin} overlaid with the

SCUBA-2 850 μm emission of Orion A, highlighting the well-known fact that the most active part of the ISF tends to be noticeably warmer than its surroundings. We note that for the GAS DR1, all spectra are fit with a single velocity component. A visual inspection of the spectra suggest that a single velocity component is sufficient to describe the majority of NH_3 spectra, even in Orion A, however, several percent of the spectra require a second velocity component to be well-described (Friesen & Pineda et al. 2017). Multiple velocity component fits are planned for a future GAS data release.

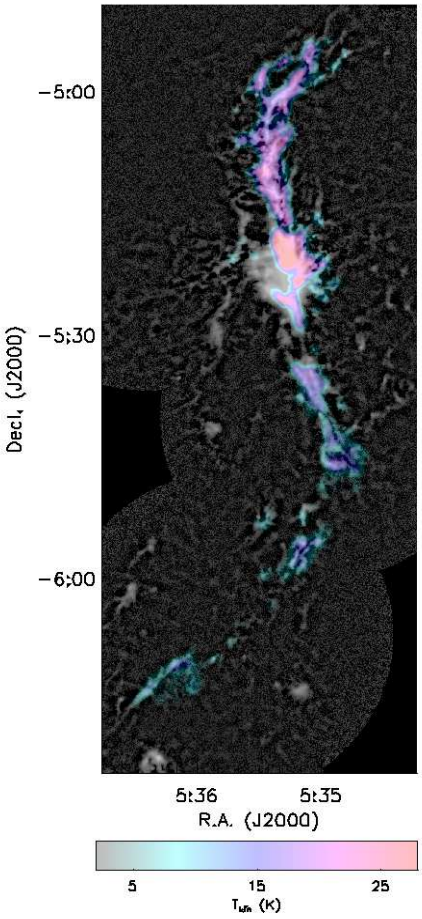

Figure 2. A comparison of the GBS 850 μm data in Orion A (greyscale) with the kinetic temperature of NH_3 fitted to the GAS data (colourscale). The SCUBA-2 flux scale is the same as in Figure 1, while T_{kin} varies from 5 K (blue) to 30 K (red) in the colour scaling (see colour bar).

Using the GAS NH_3-based property maps, we calculate the weighted mean kinetic temperature and velocity dispersion of each dense core. For the *getsources*-based dense core catalogue used for the bulk of our analysis, we consider all GAS pixels which lie within a radius of one core FWHM from each core's peak (i.e., the same area as the core's full extent, as discussed in Section 2.2), and calculate the weighted mean of each property (weighting by the inverse square of the uncertainty in the fitted parameter). We calculate both the error in the weighted mean as well as the weighted standard deviation, to measure the variation in property values across each core. These values are all

listed in Table 1. We also measured the kinetic temperature and line width at the peak position for all of the cores, and found largely similar results to those presented here. A total of 29 protostars and 282 starless cores lie within the GAS observing footprint. Of these, 26 protostars and 211 starless cores have kinematic properties measured, i.e., there was sufficient sensitivity in the ammonia data to estimate line width and kinetic temperatures. The velocity dispersions are similar for the starless and protostellar cores, with a mean and standard deviation of 0.38 km s^{-1} $\pm$0.20 km s^{-1} and 0.37 km s^{-1} $\pm$0.17 km s^{-1} for the starless and protostellar cores, respectively. The kinetic temperatures are also similar. After removing less reliable measures where $T_{kin} > 30$ K, we find typical kinetic temperatures of 18 K $\pm$ 4 K for the starless cores, and 17 K $\pm$ 3 K for the protostellar cores. Previous observations have tended to find smaller kinetic temperatures for starless cores relative to protostellar cores - for example, Jijina et al. (1999) compiled all available NH_3 observations in the literature and found median values of the kinetic temperature of 12.4 K and 15 K for apparently starless and protostellar cores respectively, while more recent work in the Perseus molecular cloud, reveals typical kinetic temperatures of 10.6 K and 11.9 K for starless and protostellar cores respectively (Foster et al. 2009). Both Jijina et al. (1999) and Foster et al. (2009) also note that environment appears to play a stronger role than protostellar content on the kinetic temperature. Jijina et al. (1999) found median kinetic temperatures of 20.5 K and 12.0 K for cores within and outside of clusters, while Foster et al. (2009) measured typical kinetic temperatures of 12.9 K and 10.8 K, for clustered and unclustered cores respectively, in Perseus. Since all of the dense cores we analyze in Orion A lie within a highly clustered environment, we might not expect to see cores with lower kinetic temperatures. This general trend of higher kinetic temperatures being present in more clustered environments is also obvious across the four GAS DR1 regions (Friesen & Pineda et al. 2017), where the isolated B18 (Taurus) has the lowest kinetic temperatures, and the moderately clustered NGC1333 (Perseus) and L1688 (Ophiuchus) have intermediate kinetic temperatures. It is possible that our estimated T_{kin} values in Orion A are also are slightly elevated due to contamination from the warmer envelope material surrounding the dense cores.

2.5. *Total Column Density*

To estimate the ambient pressure due to the weight of surrounding molecular cloud material on the dense cores, we require a map of the total column density in Orion A. Lombardi et al. (2014) derived such a column density map by performing point-by-point modelling of the spectral energy distribution of flux measured by both the *Planck* and *Herschel* Space Telescopes. We use the 850 μm optical depth map derived in Lombardi et al. (2014), and convert into column density using the equations and constants given in their Equations 12 and 16:

$$A_K = \gamma \tau_{850} + \delta \tag{2}$$

and

$$\frac{\Sigma}{A_K} = \mu \beta_K m_p \tag{3}$$

where A_K is the extinction in the K-band, $\gamma = 2640$ mag, $\delta = 0.012$ mag, Σ is the column density (in mass units), $\mu = 1.37$, $\beta_k = 1.67 \times 10^{22}$ cm^{-2} mag^{-1}, and $m_p = 1.67 \times 10^{-24}$ g[2]. Note that the γ and

[2] We note that these equations assume that there is no grain growth, a process that might affect the scaling at the highest column densities.

δ factors are fitted by Lombardi et al. (2014), and they obtain slightly different values in Orion B than in Orion A. We adopt the Orion A values here. The left panel of Figure 3 shows the column density map from Lombardi et al. (2014) with the scalings above adopted.

Every position in the column density map may have contributions from structures on a variety of size scales. To estimate the pressure on the cores from the weight of the overlying molecular cloud, we need to consider only the portion of the column density that is attributable to larger-scale structure. In particular, the 36″ angular resolution of the column density map (matching the *Herschel* resolution at 500 μm) is comparable to the size of the dense cores, suggesting that in the vicinity of the dense cores, a non-negligible portion of the column density measured could arise from the cores themselves and not larger-scale structures. We therefore filter out the smallest scale structures from the column density map when estimating the cloud weight pressure. To perform this filtering, we use a similar method to that in Kainulainen et al. (2014). Namely, we use the *a Trous* wavelet transform to measure the amount of structure on various scales[3]. Structures are measured on scales of 2^N pixels, by smoothing and subtracting the smoothed image from the remainder, going from the largest to the smallest scale. The large-scale structure can then be represented as the sum of all single-scale structure maps at sizes above the desired smoothing scale.

In the Lombardi et al. (2014) maps, each pixel is 15″, corresponding to 0.03 pc at a distance of 415 pc. Dense cores tend to have sizes between 0.03 pc and 0.2 pc (Bergin & Tafalla 2007), while larger-scale clumps and clouds span sizes from several tenths of a parsec to more than ten parsecs. For a conservative estimate, we assume that the structures of order 0.5 pc and larger belong to the cloud rather than the dense core. The closest smoothing scale to 0.5 pc is 16 pixels, which corresponds to 0.48 pc. For our nominal best estimate of the column density attributable to the cloud, we sum all structures of sizes $\sim$0.5 pc and larger generated by the *a Trous* algorithm. In Appendix B, we show that our qualitative conclusions remain similar even when we change the limiting size scale for the cloud column density features. Figure 3 shows the original Lombardi et al. (2014) column density map, as well as the 0.5 pc filtered version of the column density map, which we use for the majority of our analysis.

Within the large-scale cloud structure, dense cores are also usually found to reside within filaments. Observations from *Herschel* suggest that filaments have widths of order 0.1 pc (Arzoumanian et al. 2011; André et al. 2014), similar to the size of the dense cores, which makes separating cores and filaments unfeasible using the simple filtering method described above. In our analysis in Section 3.3, we approximate the bounding pressure of filaments using a different method than that discussed here. Finally, we note that not all of the column density may belong to structures that the core is associated with, i.e., some of the column density may belong to additional structures along the line of sight. This is especially important to acknowledge in a region as complex as Orion A. While multiple structures along the line of sight are likely more common at intermediate size scales than the largest cloud scale, we note that our estimate of the cloud column density may be slightly over-estimated.

3. ANALYSIS

3.1. *Linewidth-Size Relationship*

[3] We use the IDL program *atrous.pro* developed by Erik Rosolowsky which is available at `https://github.com/low-sky/idl-low-sky/tree/master/wavelet`.

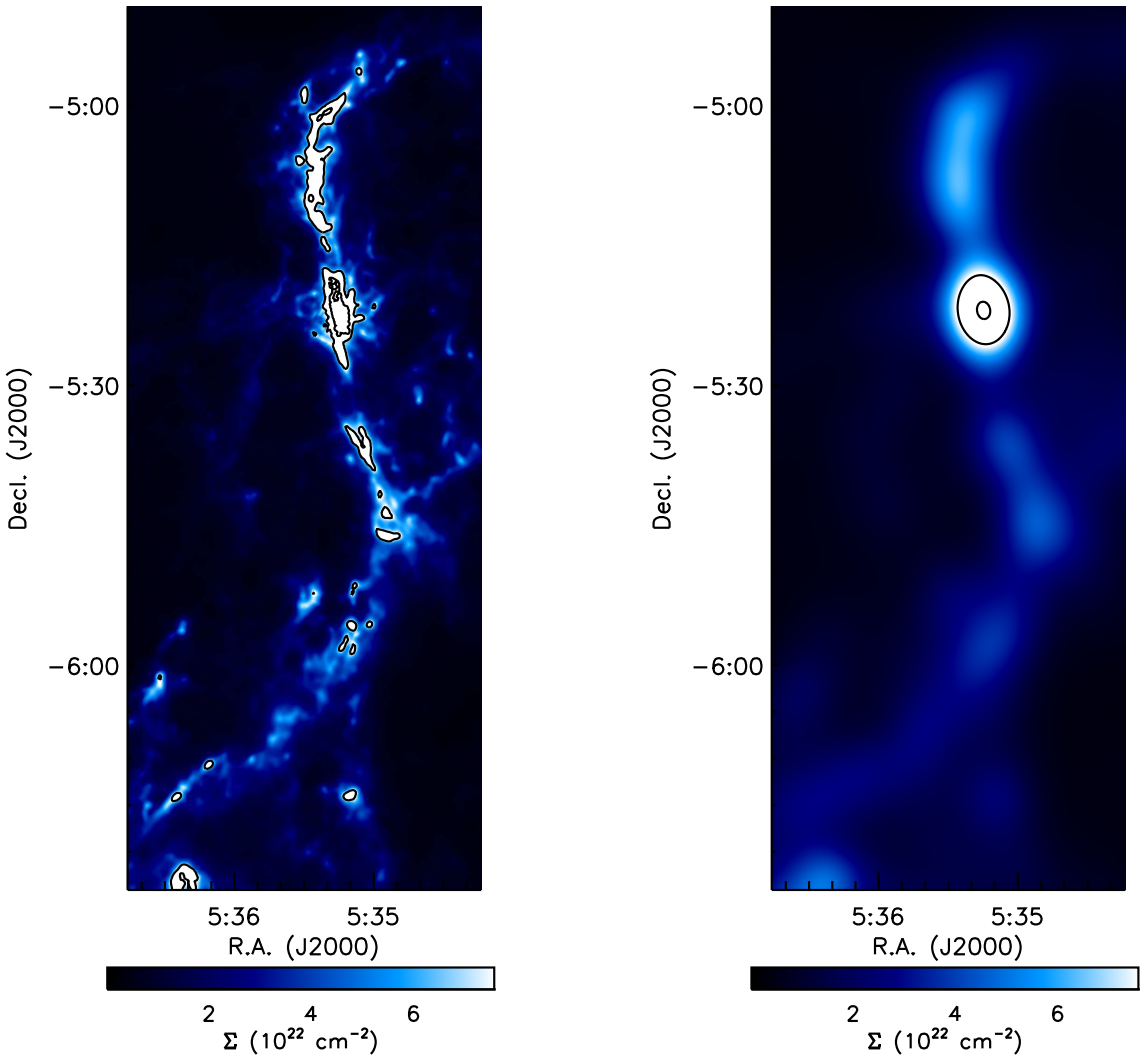

Figure 3. Left: Original column density map from Lombardi et al. (2014) shown over the same area as the previous figures. Contours are shown for 8×10^{22} cm^{-2} and 3×10^{23} cm^{-2}. Right: column density map containing only structures larger than 0.5 pc. Contours are shown for 8×10^{22} cm^{-2} and 1.2×10^{23} cm^{-2}.

We first examine the relationship between the line widths and sizes of the dense cores. The observed line width, σ_{obs} has contributions from both turbulent and thermal energy, i.e.,

$$\sigma^2_{obs,NH3} = \sigma^2_{turb} + \sigma^2_{therm,NH3} \tag{4}$$

We assume that the kinetic temperature for the mean gas is the same as we measure for NH_3, and calculate the total line width by subtracting the thermal contribution from NH_3 and adding in the assumed total gas thermal contribution, i.e.,

$$\sigma_{tot} = \sqrt{\sigma^2_{obs} - \frac{k_B T_{kin}}{\mu_{\rm NH3} m_{\rm H}} + \frac{k_B T_{kin}}{\mu_{\rm mean} m_{\rm H}}} \tag{5}$$

where k_B is the Boltzmann constant, $\mu_{\rm NH3}$ is the molecular weight of NH_3 (17), $\mu_{\rm mean}$ the mean molecular weight, and $m_{\rm H}$ the mass of a hydrogen atom. Following Kauffmann et al. (2008), we take $\mu_{\rm mean} = 2.37$.

Bulk motions within a core can also contribute to the total velocity dispersion, and are usually quantified through measurement of the standard deviation in the centroid velocity of the gas measured across the core. This contribution would then be added to the total velocity dispersion in quadrature. We find that including this term typically has a small effect on the resulting total velocity dispersions, adding less than 0.1 km s^{-1} to the total velocity dispersion calculated without its inclusion for more than 90% of the cores. The mean difference in the total velocity dispersion between including and excluding the standard deviation in centroid velocity is 0.04 km s^{-1}, while the median difference is 0.02 km s^{-1}. We therefore exclude the contribution from the change in line centroid to the total velocity dispersion that we use for our analysis.

Figure 4 shows the total line width and size measured for each core, using Equation 5. All of the cores have significantly supersonic velocity dispersions – the velocity dispersion expected for a purely thermal gas at the mean T_{kin} value observed is shown by the horizontal dashed line, and it lies about a factor of two lower than the smallest total velocity dispersions measured. These line widths are larger than is typical for the nearest molecular clouds, such as those in Perseus, where cores tend to have roughly transsonic total line widths (e.g., Foster et al. 2009). Orion, however, has long been recognized as an environment where cores have larger non-thermal motions present in dense gas tracers such as NH_3 (e.g., Jijina et al. 1999; Caselli & Myers 1995). These larger line widths do not appear to be an artefact of the larger distance to Orion as compared to nearby clouds such as Perseus. We compared the NH_3 line widths reported by Li et al. (2013) using higher angular resolution VLA observations ($\sim$5″ versus our 32″) and see no evidence that our measured line widths are systematically larger. On the contrary, our measurements tend to be slightly smaller, likely due to the poorer velocity resolution of the observations of Li et al. (2013).

The dotted diagonal line in Figure 4 shows the standard Larson (1981) line width-size relationship measured for larger-scale structures using CO observations. Clearly our population of cores does not follow Larson's scaling law, but instead shows no variation as a function of core size, and only a large amount of scatter. This lack of change in line width as a function of size is exactly what is expected for the behaviour of dense gas within cores, as the material lies in a zone of coherence (e.g., Goodman et al. 1998; Pineda et al. 2010), although the zone of coherence is typically also characterized by a thermally-dominated velocity dispersion, which is not the case here.

3.2. *NH_3 motions versus self-gravity*

We next compare the amounts of thermal and non-thermal support available to each dense core to their self-gravity. The thermal Jeans criterion is:

$$M_{J,T} = \frac{5R}{2G(\mu_{\rm mean} m_{\rm H}/k_B T_{kin})} \tag{6}$$

(e.g., Bertoldi & McKee 1992) where $M_{J,T}$ is the (thermal) Jeans mass, R is the radius, and G is the gravitational constant. If non-thermal support is included, we can re-write the equation as

$$M_{J,tot} = \frac{5R\sigma_{tot}^2}{2G} \tag{7}$$

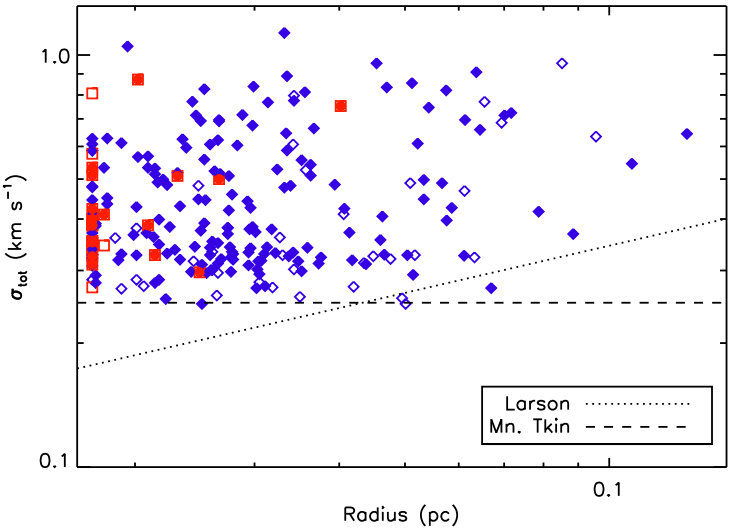

Figure 4. The total 1-D velocity dispersion of the dense cores compared with their effective radii. The dashed horizontal line shows the velocity dispersion of purely thermal gas at a temperature equal to the mean kinetic temperature of the cores, i.e., 18 K. The dotted diagonal line shows the line width-size relationship reported by Larson (1981), after scaling for the appropriate observed quantities, i.e., radius versus diameter and 1-D versus 3-D velocity dispersion. Red squares indicate protostellar cores while blue diamonds indicate starless cores. Filled symbols indicate cores lying near the ISF, and open symbols show cores which lie further south.

where σ_{tot} is the total line width given by Equation 5.

Figure 5 shows the mass and size measured for each dense core based on SCUBA-2 850 μm data compared to various Jeans stability criteria. Here, we use the mean values of T_{kin} and σ_{nt} obtained for dense cores where a good fit to these parameters was obtained. Unsurprisingly, turbulent motions dominate over thermal motions in all cores. When non-thermal motions are considered in addition to the thermal pressure supporting the dense cores, nearly all of the dense cores lie below the Jeans line (dashed line in the figure). This behaviour implies that the cores are gravitationally unbound, i.e., they have insufficient self-gravity due to their mass to counteract the internal (turbulent) gas motions.

In Figure 6, we show σ_{tot} versus σ_{grav}, the dispersion needed to balance gravity alone, to make a similar comparison on a core-by-core basis and account for variations in the T_{kin} and σ_{tot} measured for each core. Here too, the final result is similar: most of the cores do not have sufficient mass to remain bound.

The cores that are gravitationally bound tend to have larger masses. The virial ratio, defined as

$$\alpha = \frac{5\sigma_{tot}^2 R}{GM} \tag{8}$$

represents the degree to which a core is gravitationally bound, with bound cores satisfying $\alpha < 2$ (e.g., Bertoldi & McKee 1992). Figure 7 shows the virial parameter as a function of core mass, showing that the most massive cores are the ones most likely to be gravitationally bound. Similar behaviour has been seen in other studies of populations of dense cores, such as the Pipe Nebula (Lada et al. 2008).

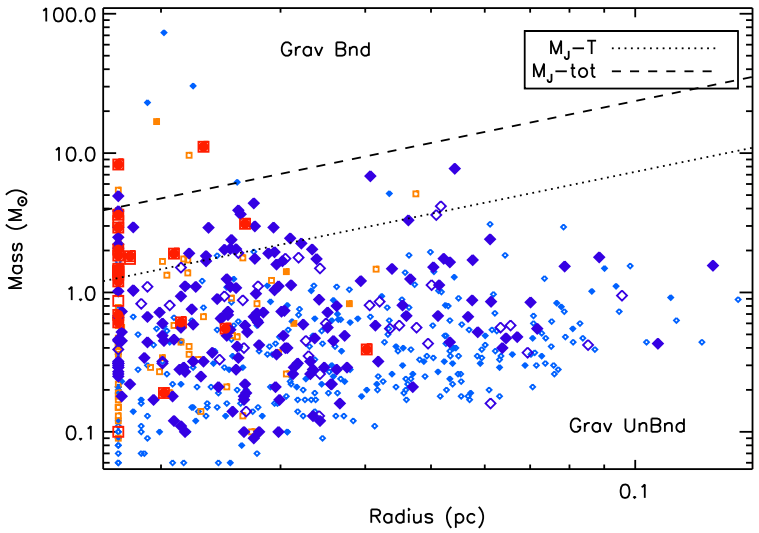

Figure 5. A comparison of the masses and sizes of the dense cores. Starless cores are shown as blue diamonds while protostellar cores are shown as red squares. Filled symbols show cores associated with the ISF MST-based cluster in Lane et al. (2016). The dotted line indicates the thermal Jeans mass for the mean temperature measured for the cores. The dashed line shows the Jeans mass when mean non-thermal motion is included as a thermal pressure-like term. Smaller, lighter symbols show cores that fell within the GAS footprint but did not have reliable kinematic properties measured.

Although the trend that we observe in virial ratios decreasing with increasing core mass is consistent with previous studies, it is worth noting that most nearby dense core populations such as Perseus tend to have overall lower virial ratios than what we measure (e.g., Kirk et al. 2007; Foster et al. 2009). There are several reasons that dense cores in Orion could appear to be less self-gravitating than in nearby clouds: 1) the larger distance to Orion could lead to a greater confusion of multiple velocity components within the telescope's beam, artificially increasing the measured core velocity dispersions; 2) the higher mean density in Orion could imply that NH_3 traces kinematics beyond the core, implying that the NH_3 velocity dispersion is larger than should be attributed to the core; or 3) Orion does truly harbour more non-self-gravitating cores.

We can rule out the first possibility through comparison with Li et al. (2013). Li et al. (2013) use a combination of VLA and GBT NH_3 observations to assess the virial state of dense cores in the OMC2 and OMC3 regions of Orion A. There, the angular resolution is 5″ and the velocity resolution is 0.6 km s^{-1}. We compared the reported velocity dispersions for cores at nearly coincident positions in Li et al. (2013) and our own work, and found that our velocity dispersions tended to be slightly smaller. The relatively poor velocity resolution in the Li et al. (2013) observations likely causes slight over-estimates in their velocity dispersion measurements. The fact that we observe slightly lower core velocity dispersions, however, suggests that the spatial resolution of our GBT observations does not cause a significant increase to the velocity dispersions that we report. Further comparisons with the Li et al. (2013) results are discussed in Section 3.6.

The second possibility requires observations using a higher effective density molecular tracer (e.g., Shirley 2015). Ideally, such a tracer would be known to trace unambiguously much denser gas than NH_3, such as a deuterated form of ammonia (e.g., Crapsi et al. 2007). The closest observations

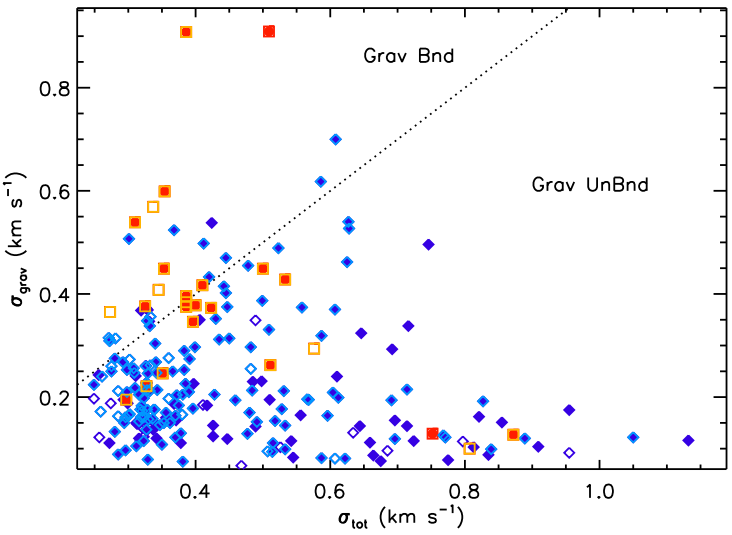

Figure 6. A direct comparison of the velocity dispersion required to balance gravity (vertical axis; σ_{grav}) with the total velocity dispersion measured (horizontal axis). Blue diamonds denote starless cores while red squares denote protostellar cores. Filled symbols show cores associated with the ISF, while open symbols show cores which are located further south in Orion A. Cores with lighter outlines have upper limits to their true sizes reported, implying that the estimated values of σ_{grav} are lower limits. Cores lying below the dotted line are gravitationally unbound. Both this figure and Figure 5 clearly indicate that considering only the balance between gravity versus temperature and local non-thermal motions implies that most of the dense cores are gravitationally unbound.

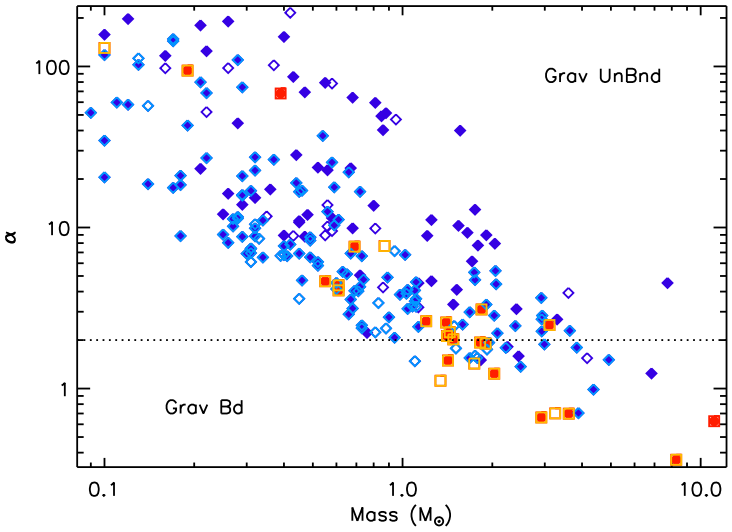

Figure 7. A comparison of core masses and their estimated virial parameters. As in previous figures, blue diamonds denote starless cores while red squares denote protostellar cores. Filled symbols show cores associated with the ISF, while open symbols show cores which are located further south in Orion A. Cores with lighter outlines have upper limits to their true sizes reported, implying that the estimated values of α are also upper limits. Cores lying above the dotted line are gravitationally unbound.

that we were able to find to satisfy this condition use N_2H^+. N_2H^+ has a higher effective density than NH_3 (Shirley 2015), and NH_3 appears to be sensitive to gas at lower densities than N_2H^+. For example, the lower-density filament B216 in Taurus is visible in NH_3 but not N_2H^+ (Seo et al. 2015). Due to a combination of chemical and optical depth effects, however, NH_3 *also* traces gas to higher densities than N_2H^+ – e.g., see the higher concentration of core emission in NH_3 relative to N_2H^+ in Tafalla et al. (2002) and the simulations of Gaches et al. (2015). While a full understanding of the chemistry behind the creation and destruction for both N_2H^+ and NH_3 remain elusive (see Caselli et al. 2017, for a recent test of models of the latter), observations such as those described here are strong evidence that NH_3 traces a wider range of densities than N_2H^+. Therefore, while N_2H^+ is not strictly a tracer of denser gas than NH_3, comparison between the two should allow us to test whether or not a significant amount of the NH_3 emission originates from the lowest densities of material to which it is sensitive. We note that if the mean density in Orion is sufficiently high that even N_2H^+ is sensitive to inter-core gas, as has been found in some infrared dark clouds (IRDCs; e.g., Henshaw et al. 2013), then this comparison between NH_3 and N_2H^+ will not rule out the possibility of contamination in the NH_3 spectra from non-core gas.

Tatematsu et al. (2008) observed the N_2H^+ (1-0) emission line in OMC2 and OMC3 using the Nobeyama Radio Observatory, with a spatial resolution of 17″ (with a spacing between observations of 41.1″) and a velocity resolution of 0.12 km s^{-1}. We compared the N_2H^+ velocity dispersion reported by Tatematsu et al. (2008) with the NH_3 velocity dispersion that we measure at the same locations of a sample of their cores with a range of declinations and find very good agreement, always within 0.02 km s^{-1}. This close correspondence in velocity dispersions implies that the NH_3 and N_2H^+ are tracing similar zones of material. Furthermore, a visual comparison of on-core and nearby off-core NH_3 spectra suggest that the core emission is not being significantly biased to higher widths due to non-core material. While these tests suggest that the NH_3 emission is not dominated by material at the lowest densities to which it is sensitive, observations of an unambiguously higher density tracer, such as emission from deuterated NH_3, should be used to verify this behaviour.

With the data available, we argue that it is reasonable to assume that the cores in Orion A represent a truly less self-gravitating population than is typically observed in nearby molecular clouds. The less self-gravitating cores certainly do not appear to be due to observational biases due to the greater distance to Orion A. Observations of a high density molecular tracer on small spatial scales are necessary, however, to verify that the large line widths originate in gas associated with the dense cores.

3.3. *Pressure*

3.3.1. *Cloud Weight*

We next modify our analysis to include the fact that the ambient molecular cloud material provides an additional confining pressure on the cores. Under the assumption that the large-scale cloud can be roughly approximated by a sphere, the column density at the position of each core then provides an estimate for how deeply embedded the core is within the cloud. Although the Orion A cloud is clearly not spherical, we argue that the approximation is acceptable for the large-scale column density distribution, since, as we discussed in Section 2.5, we already exclude small-scale column density features from consideration. The pressure exerted on the ambient cloud is often expressed as

$$P_{cloud} = \pi G \bar{\Sigma} \Sigma \tag{9}$$

where P is the pressure, $\bar{\Sigma}$ is the mean cloud column density, and Σ is the column density at the location of the dense core (see, for example, Kirk et al. 2006; McKee 1989). As we show in Appendix C, this equation is strictly appropriate only for a spherical cloud with density varying as $\rho \propto r^{-k}$ with $k = 1$. Other values of k in the density scaling lead to a two-term expression for the pressure, given in Equation C2. When the cloud's density distribution has an exponent of $1 < k < 3$, a reasonable range for large-scale clouds, this second term is positive, so Equation 9 provides a lower limit to the full pressure. Additional considerations, such as using $\Sigma/2$ as a proxy for how deeply embedded a dense core is within the cloud, may introduce some bias to the cloud weight pressure estimate when $k \neq 1$. See Appendix C for further discussion of the caveats associated with estimating the cloud weight pressure.

To calculate the mean cloud column density used in Equation 9, we consider only the area within the large-scale column density map which was covered in the GAS observations, yielding a value of $\bar{N} = 3.9 \times 10^{22}$ cm^{-2} or $\bar{\Sigma} = 8.9 \times 10^{20}$ g cm $^{-2}$.

To compare the relative strengths of cloud pressure, core self-gravity, and thermal plus non-thermal support, we use the formalism introduced in Pattle et al. (2015), expressing each in terms of their energy density in the virial equation:

$$\Omega_P = -4\pi P R^3 \tag{10}$$

$$\Omega_G = \frac{-1}{2\sqrt{\pi}} \frac{GM^2}{R} \tag{11}$$

$$\Omega_K = \frac{3}{2} M \sigma_{tot}^2 \tag{12}$$

where Ω_P is the pressure term, Ω_G is the gravitational term, and Ω_K is the kinetic term. The expression for Ω_G is derived in Pattle (2016) for a core with an infinitely extending Gaussian density distribution. For a core with Plummer-like density distribution (e.g., Whitworth & Ward-Thompson 2001)[4] with an exponent of 4, the factor of $\sqrt{\pi}$ becomes π instead, i.e., implying slightly smaller Ω_G values than we estimate. For a constant density object, as is assumed when deriving the standard virial parameter or Jeans mass discussed earlier, Ω_G is a factor of ~ 3.5 larger. A dense core is in virial equilibrium when $-(\Omega_G + \Omega_P) = 2\Omega_K$.

In Figure 8, we show the energy density ratio for the dense cores, compared to the ratio of the gravitational and pressure energy densities. The latter ratio expresses whether gravity or pressure is the dominant element binding the core, and is termed the 'confinement ratio' in Pattle (2016). As can be seen in Figure 8, the majority of dense cores are bound, with energy density ratios exceeding one. As already illustrated in Figure 6, self-gravity alone contributes relatively little to this binding; pressure dominates gravity for the vast majority of the cores. A trend of decreasing confinement ratio with increasing energy density ratio is seen in Figure 6. We investigated the cause of this trend, and found no correlation between $\Omega_{P,cloud}$ and either Ω_K or Ω_G. Ω_G, however, varies approximately as Ω_K^2. This latter trend appears to be driven by the mass term in Ω_G and Ω_K, which follows the same relative scaling. As Figure 4 has already shown, there is no relationship between R_{eff} and σ_{tot}, and both have a relatively small range in values (approximately an order of magnitude). The range of

[4] A Plummer-like column density distribution has $\Sigma \propto \left(\frac{R_{flat}}{\sqrt{r^2+R_{flat}^2}}\right)^{\eta}$ where R_{flat} is the radius of the central flat portion of the core and η describes the outer power law slope (see Pattle 2016, for more information).

masses is just over three orders of magnitude, and thus appears to be driving the correlation between Ω_K and Ω_G, which in turn is responsible for the trend seen in Figure 6.

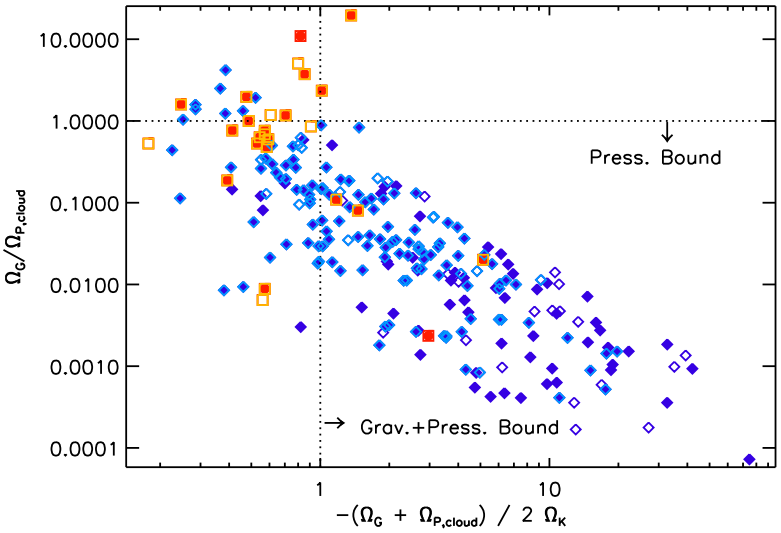

Figure 8. A comparison of terms in the virial equation, following Pattle et al. (2015). The vertical axis shows the ratio of self-gravity to pressure, i.e., the confinement ratio, showing that in most cores, pressure plays a more significant role in binding the cores than gravity does. The horizontal axis shows the ratio of energy densities with cloud pressure included. Inclusion of cloud pressure causes most of the dense cores to be bound, with the majority of that binding attributable to the weight of the overlying cloud material. See Figure 6 for the plotting conventions used.

3.3.2. *Filament Pressure*

As discussed in Section 2.5, cores are typically found embedded within filaments in the larger molecular cloud structure. Like the larger molecular cloud, these filaments will also help to confine the dense cores. Since it is difficult to disentangle the column density belonging to the filaments and the dense cores with simple techniques due to their similar size scales, we instead use previous observations to estimate a lower limit to the filament confining pressure. Tafalla & Hacar (2015) observed filaments and cores in the Taurus L1495/B213 region using a combination of dust continuum and molecular emission line observations. They used these observations to model the density profile of the filaments in locations where cores were not present, using a cross sectional profile of

$$n(r) = \frac{n_0}{1 + (r/r_0)^{\alpha}} \tag{13}$$

where n is the density at radial separation r, n_0 is the central density, r_0 is the characteristic size, and α is the power law dependence (Whitworth & Ward-Thompson 2001). Across eight different filaments in Taurus, Tafalla & Hacar (2015) find $n_0 \sim 6.5 \times 10^4$ cm^{-3}, $r_0 \sim 45$ ″ (at an assumed distance of 140 pc), and $\alpha \sim 3$, while a characteristic temperature of 10 K was assumed.

The pressure induced by the weight of overlying material in an isothermal filament can be expressed as

$$P_{fil} = \frac{2}{\pi} G \Sigma_{\perp}^2 \tag{14}$$

(see Appendix C) where $\Sigma_\perp$ is the column density through the centre of the filament. The binding pressure on cores from the filaments measured in Taurus can therefore be estimated using the Tafalla & Hacar (2015) model estimates. Filaments in Orion, however, are likely to be much more dense than those found in Taurus, and therefore the Taurus estimate provides us with a lower limit to the true filament pressure. Generally, the pressure exerted by the cloud on cores is about a factor of 10 higher than the pressure exerted by these model filaments. Figure 9 shows the resulting energy density ratios with this additional pressure included (see also the following section for a further pressure term added).

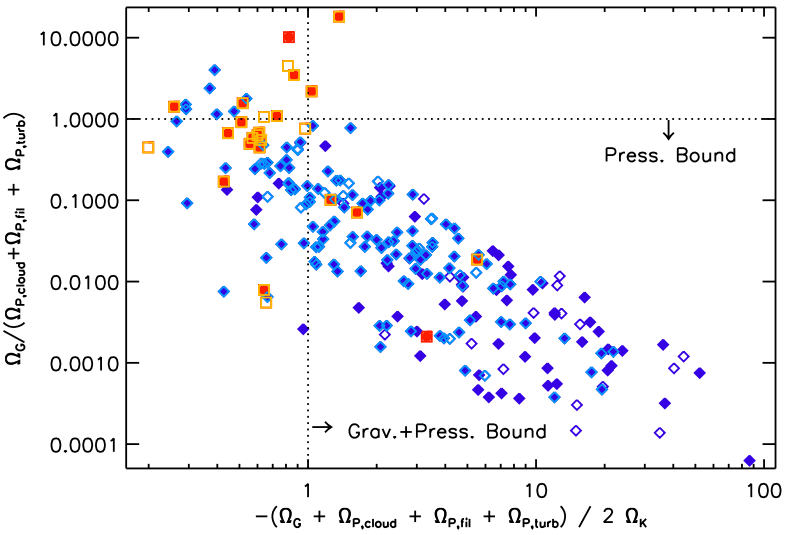

Figure 9. A comparison of terms in the virial equation, similar to that shown in Figure 8. Here, Ω_P includes the cloud weight pressure, filament weight pressure, and turbulent pressure. See Figure 6 for the plotting conventions used.

3.3.3. *Turbulent Pressure*

In addition to the weight of overlying material, turbulent pressure, i.e., pressure induced from the higher velocity dispersion, lower column density material surrounding the cores, may also be present. We estimate the magnitude of this pressure in an approximate way. Shimajiri et al. (2014) obtained ^{13}CO (1–0) and C^{18}O (1–0) observations of the northern portion of Orion A, extending slightly southward of the main ISF. According to their Figure 2, the C^{18}O (1–0) emission has a velocity dispersion < 1.5 km s^{-1} everywhere, with most of the gas having velocity dispersions < 0.75 km s^{-1}. They assume a mean density of material traced by C^{18}O (1–0) emission of 5×10^3 cm^{-3}, based on previous analysis by Ikeda & Kitamura (2009). Using these estimates, the turbulent pressure on the dense cores can be written as

$$P_{turb} = \rho_{turb}\ \sigma^2_{v,turb\ gas} \tag{15}$$

(e.g., Pattle et al. 2015). A more careful measurement of both the mean gas density and typical CO velocity dispersion around each dense core (or even the velocity dispersion of the surrounding fainter NH_3 emission) would be required to obtain a more precise estimate of the turbulent confining pressure. Nonetheless, using the present equation to approximate the influence of turbulent pressure

in combination with the filament weight pressure discussed above, Figure 9 shows that all cores have slightly increased energy density ratios, with an additional six dense cores now appearing to be bound. We emphasize that more precise, core-specific, estimates for both the turbulent pressure and the filament weight pressure could yield additional binding, especially as the latter pressure estimate is a lower limit.

3.3.4. *Bonnor-Ebert Sphere Pressure*

Cores are often approximated as Bonnor-Ebert spheres (Ebert 1955; Bonnor 1956), a spherically symmetric, isothermal equilibrium model where self-gravity and an external binding pressure balance internal thermal motions. In this model, the maximum external binding pressure for a stable BE sphere model can be expressed as

$$P_{BE,crit} = 1.40 \frac{c_s^8}{G^3 M^2} \tag{16}$$

(Hartmann 1998). While we do not find any correlation between the critical binding pressure of a BE sphere and the estimated pressure on each core from the weight of the overlying cloud material, the values span a similar range. The mean and standard deviation of $log(P_{BE,crit}/k_B)$ is 6.5 ± 0.8 log(K cm^{-3}). This rough similarity in pressures between the BE sphere model and those estimated from the weight of the cloud suggest that the BE sphere model may provide a reasonable representation of the cores, although this conjecture should be tested more carefully through measurements of the radial column density profile of the cores.

3.4. *Concentration*

When only dust continuum information is available for cores, often their stability is assessed in terms of their concentration, or peakiness. Following Johnstone et al. (2001), the concentration, C, can be written as

$$C = 1 - \frac{1.13 B^2 S_{tot}}{\pi R^2 F_{pk}} \tag{17}$$

where B is the telescope beamsize, S_{tot} is the total flux observed, and F_{pk} is the peak flux density observed. Typically, B is expressed in arcsec, S_{tot} in Jy, R in arcsec, and F_{pk} in Jy beam^{-1}. In the BE sphere model, when observed in 2D, the minimum concentration is 0.33, representing a uniform density sphere, while the maximum concentration for a stable configuration is 0.72 (Johnstone et al. 2000). In Figure 10, we show the concentration measured for each dense core compared to its respective energy density ratio. Higher concentration cores have more mass within a smaller size, and therefore would be expected to have stronger self-gravity, and hence a higher energy density ratio. As plotted in Figure 10, there is an absence of low-concentration strongly bound cores and high-concentration strongly unbound cores, both of which represent states that would be difficult to populate or maintain. There is no further correlation visible between the two quantities.

Some of the protostellar cores have low concentration values. Previous studies, such as van Kempen et al. (2009), have found low concentration protostellar cores when the core evolution is more advanced, i.e., much of the core material has already been accreted onto the central protostar or dispersed by protostellar outflows, making the remaining envelope traced by the submillimetre continuum observations appear more diffuse. Angular resolution and the core identification algorithm used also play a role in the concentrations observed, since both of these influence the peak and total flux associated with each core.

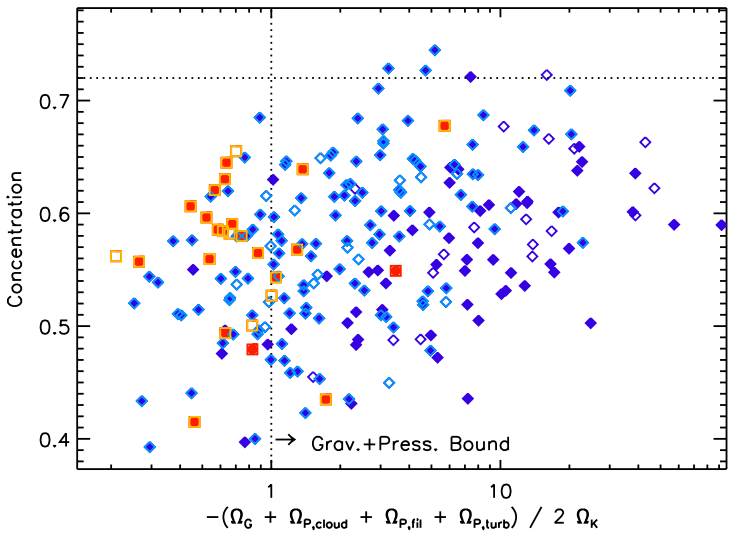

Figure 10. A comparison of the central concentration of the dense cores with their energy density ratio as shown in Figure 8. The horizontal dotted line marks the maximum stable concentration for the BE sphere model, while the vertical dotted line denotes the boundary between bound (right) and unbound (left) systems. Note that very few of the dense cores have concentrations exceeding that expected for a stable Bonnor Ebert sphere model. See Figure 5 for the plotting conventions used.

3.5. *Regional Variation*

We additionally checked whether or not there are any bulk differences in the virial properties of dense cores associated with the ISF and the remainder of the field. Lane et al. (2016) identified clusters of dense cores across Orion A using minimal spanning trees. One of these clusters roughly encompasses the ISF, and therefore provides a simple way to identify dense cores either associated or not associated with the ISF. In all of the previous figures showing dense core properties, filled symbols denote cores associated with the ISF, while open symbols show cores not associated with the ISF. Dense cores associated with the ISF tend to have slightly smaller energy density ratios than the remaining cores, due to their typically smaller sizes and therefore much smaller Ω_P values but the two populations largely overlap. The starless cores in the ISF have typical energy density ratios of $log(-\Omega_G - \Omega_{P,tot})/2\Omega_K = 0.39 \pm 0.42$, while the starless cores outside of the ISF have typical values of 0.62 ± 0.42 (median and median absolute deviation quoted for both). The non-ISF population that we analyze is presently small (39 starless cores), but the full GAS map of Orion A will extend much further south than the DR1 map analyzed here, and will allow for a more stringent test of whether or not virial properties vary between the ISF and the rest of Orion A.

3.6. *Comparison to Li et al. (2013)*

As noted in Section 3.2, Li et al. (2013) observed NH_3 in cores in the Orion A OMC2 and OMC3 regions and assessed their virial nature. While Li et al. (2013) also find that many of their dense cores are not self-gravitating ($\alpha > 2$), they do not report virial ratios as high as those found in our analysis. The relative lack of high virial ratios in Li et al. (2013) can be attributed to our greater sensitivity to lower mass cores. For example, almost none of the Li et al. (2013) cores have masses below 1 $M_\odot$, while more than half of our cores (65%) have masses below 1 $M_\odot$. As discussed earlier,

higher mass cores tend to be more self-gravitating, so it is reasonable that the lower mass cores in our sample have larger virial ratios than those reported in Li et al. (2013).

In their full virial analysis, Li et al. (2013) include a turbulent pressure term estimated assuming a mean gas density of 10^4 cm^{-3} and a mean velocity dispersion of 1 km s^{-1}. This implies a slightly larger turbulent pressure than the one we estimate in Section 3.3.3, which we noted is typically smaller than the pressure binding provided by the overlying cloud material that we estimated for each core individually. Li et al. (2013) also include a magnetic support term in their analysis, assuming a typical field strength of 0.1 mG based on nearby observations of the Zeeman effect in CN. Including both the turbulent pressure binding and magnetic support reduces the number of super-virial cores in their analysis, although nearly half (47%) of their cores still appear to be unbound, with a 'critical mass ratio' above one. The overall conclusions of Li et al. (2013) therefore seem consistent with our own results, given the different core samples and different assumptions used for the virial analysis.

New results from the BISTRO survey (Ward-Thompson et al. 2017) suggest that the total magnetic field strength may be substantially larger than assumed in the Li et al. (2013) analysis. Using the Chandrasekhar-Fermi method (Chandrasekhar & Fermi 1953), Pattle et al. (2017) estimate a magnetic field strength in the OMC-1 region, i.e., the central densest portion of the ISF) to be 6.6±4.4 mG in the plane of the sky. At this level, the magnetic field would contribute significantly to the energy density of each core. Inclusion of the magnetic pressure would serve to increase the amount of internal support against the gravitational collapse of the cores, thus in Figure 9, points would move up and to the left. The magnetic pressure may not be well-approximated by a constant field strength value over the large area of Orion A included in our analysis, as the field strength derived only for the densest part of the cloud may not be representative of the entire region. Therefore, while we exclude the magnetic support term from our virial analysis, we note that this should be re-visited when magnetic field strength estimates are available for a larger extent of Orion A.

4. DISCUSSION

The potential for dense cores to be pressure-bound due to the weight of the overlying molecular cloud material has been considered for several decades (e.g., Elmegreen 1989; Bertoldi & McKee 1992), and some early observations supported this hypothesis (e.g., Keto & Myers 1986). Other types of external pressure have also been considered, including inter-core ram pressure (Miettinen et al. 2010), ram pressure generated by core accretion (Naranjo-Romero et al. 2015; Seo et al. 2015), radiation pressure (Seo & Youdin 2016), and turbulent shocks (Gong & Ostriker 2015). A related issue is the role of tidal forces within molecular clouds. As discussed in Ballesteros-Paredes et al. (2009), tidal disruption should be considered for a full virial analysis of molecular clouds. On the scale of cores, however, tidal compression is more likely than tidal disruption, and is generally expected to contribute less than self-gravity for smaller cores. We therefore expect tidal effects to increase slightly the total number of bound cores in our sample. Beyond the role of external pressure, whether dense cores are in stable equilibrium, unstable equilibrium (e.g., Field et al. 2011), or not in equilbrium at all, as suggested by some numerical simulations (e.g., Ballesteros-Paredes et al. 2003; Naranjo-Romero et al. 2015), is an additional issue to consider. Our analysis makes the simplest and usual assumption that the dense cores evolve sufficiently slowly that the virial equation parameters measured provide a reasonable approximation of the full virial state of the cores.

On the kinematic side, we made the simple assumption that the entire velocity dispersion of the core acts to provide internal thermal plus non-thermal pressure support. While this assumption is

reasonable for the thermal pressure, the non-thermal velocity dispersion almost certainly does not represent only isotropic small-scale motions that provide additional pressure support. For example, some of the non-thermal velocity dispersion could be caused by infall motions within the core, which can lead to broader emission lines in dense gas tracers (e.g., Myers 2005; Bailey et al. 2015). For the protostellar cores, where we know that infall motions must be present, in addition to some of the starless cores where infall has begun but has not yet produced a detectable central protostar, the observed line widths will be larger due to infall motion (e.g., Caselli et al. 2002). Our present analysis therefore over-estimates the amount of internal pressure support, and hence under-estimates the level of binding of these cores. Mapping or pointed observations of a reliable infall tracer such as HCN (e.g., Sohn et al. 2007) could be used to help remove this bias in our analysis.

A final subtle consideration is the degree to which the column density and velocity measurements we use correspond to single discrete cores in three-dimensional space. Beaumont et al. (2013) ran a careful comparison of numerical simulations of a molecular cloud as viewed in true 3-D (position-position-position, or PPP) space versus the view inferred from synthetic ^{13}CO (1-0) observations of the position-position-velocity (or PPV) structures. They found that the lack of perfect correlation between PPP and PPV structures led to scatter in the virial parameters by a factor of about two. Since NH_3 traces denser gas than ^{13}CO, the correspondence between structures is likely moderately better, as line-of-sight confusion is expected to play a smaller role in dense gas, which has a lower volume filling fraction. Nevertheless, the high average density of Orion A allows for the possibility that some of the apparent cores in our SCUBA-2 based catalogue could be chance alignments of somewhat dense gas along the line of sight rather than representing a true core or include some contamination from the material surrounding a true core. Since our analysis requires not only NH_3 (1,1) but also NH_3 (2,2) emission for cores to be reasonably well detected (at S/N > 3), we expect that there should be a minimal number of unreal cores in our analysis, but it is possible that a few of our cores with the faintest and broadest NH_3 spectra fall into this category.

4.1. *Previous Studies With Pressure*

Our conclusion that Orion A dense cores are significantly bounded by the pressure of the surrounding cloud material is a result that has been found in other nearby molecular clouds as well, spanning a range of environments. One example is the nearby Pipe Nebula, a star-forming environment significantly different from Orion A. Dense cores in the Pipe have typical volume densities of less than 10^4 cm^{-3}, sizes of $\sim$0.2 pc, non-thermal velocity dispersions of $\sim$0.2 km s^{-1}, and inhabit a cloud with a mean extinction of $A_V \sim 4$ mag and a total mass of $\sim 10^4$ M$_\odot$ that is located a mere 130 pc away (Alves et al. 2007; Lada et al. 2008, and references therein). Lada et al. (2008) used pointed NH_3 or C^{18}O observations, in combination with dense core sizes and masses estimated using extinction mapping, to demonstrate that most Pipe dense cores have insufficient mass to be gravitationally bound. Furthermore, the vast majority of the internal pressure support in Pipe cores was found to be from thermal pressure rather than non-thermal motions. They also found a surprising similarity in the total internal pressures of Pipe cores across the cloud and argued that the most likely source of pressure on Pipe core boundaries is that caused by the weight of the overlying cloud material. Indeed, typical internal core pressures tend to be slightly larger in the 'bowl' of the Pipe, compared to the 'stem'; the former area is also associated with higher mean cloud column densities. Magnetic pressure may also play an important role in confining cores in the Pipe, as argued by Alves et al. (2008). In contrast to the Pipe, Orion A has a mean cloud column density contributing to the cloud

external pressure that is much higher (a factor of > 5), and non-thermal motions and perhaps additional sub-core bulk motions provide significant contributions to the internal pressures of its dense cores.

Several other studies examining the role of cloud pressure have been performed in star-forming regions which have properties intermediate to the Pipe and Orion A (i.e., cloud mass, dense core volume density, size, and non-thermal velocity dispersion). In the Ophiuchus molecular cloud, three independent analyses using different datasets all came to the conclusion that external cloud pressure is important in confining many cores in the cloud. Specifically, Johnstone et al. (2000) argued this point based on Bonnor-Ebert sphere modelling of dust continuum observations at 850 μm and the level of expected pressure from ambient cloud material, Maruta et al. (2010) used Nobeyama $H^{13}CO^+$ observations, while Pattle et al. (2015) used a combination of SCUBA-2 850 μm dust continuum data and IRAM 30 m N_2H^+ and $C^{18}O$ observations. In the Perseus molecular cloud, Kirk et al. (2007) analyzed the dense cores, while Sadavoy et al. (2015) analyzed the larger B1-E structure, both also finding evidence that pressure confinment is important. Note, however, that Foster et al. (2009) also analyzed Perseus dense cores and found instead that self-gravity alone was sufficient to confine the dense cores. This difference is primarily due to the larger masses derived for the dense cores by Foster et al. (2009) using CSO Bolocam data, rather than higher resolution JCMT SCUBA data of Kirk et al. (2007). Foster et al. (2009) furthermore did not estimate the magnitude of cloud pressure to see how it compares with core self-gravity, and it is likely that such an estimate would provide a larger amount of binding than they estimated from self-gravity alone. In the Taurus L1495 / B218 region, Seo et al. (2015) analyzed the virial properties of filaments and smaller structures using NH_3 observations, and found that most of the small NH_3 structures are gravitationally unbound when considering just the balance between self-gravity, and thermal plus non-thermal support. They argued that many of these structures, especially the youngest ones, appear to be pressure confined, and that cloud pressure is a reasonable candidate for the source of that pressure with ram pressure from material inflowing to the system being their other main candidate. In the Cepheus clouds, Pattle et al. (2016) performed a virial analysis using a combination of JCMT SCUBA-2 850 μm dust continuum and archival ^{13}CO observations to argue that cloud pressure is required to bind most of the dense cores. Similarly, Kirk et al. (2016) find suggestive evidence that cloud pressure is important for dense cores in Orion B, although there, the analysis lacks kinematic information to provide precise estimates of the dense cores' temperatures and non-thermal motions[5].

For more distant (non-Gould Belt) star-forming regions, Kauffmann et al. (2013) performed a self-consistent virial analysis combining observations from a variety of previous surveys. While external pressure was not included in their analysis, a comparison of self-gravity and non-thermal motions showed that the majority of structures were unbound. Structures that were bound were either much larger entities (masses above 100 $M_\odot$), or were in regions of high-mass star formation, or both. Kauffmann et al. (2013) speculate that the structures, which do appear to be gravitationally unbound, may in fact be pressure bound. Additionally, Barnes et al. (2016) analyze a large sample of massive molecular clumps observed with the CHaMP survey in HCO^+ and ^{12}CO emission to demonstrate that the less dense gas traced by ^{12}CO appears to provide significant pressure binding to the more compact clumps traced by HCO^+, at a sufficient level that most of the clumps are near

[5] GAS will provide NH_3 observations in a future data release, however.

virial equilibrium. Thus, while it may be the case that high mass stars form under a different mode, dense cores which form low- to intermediate- mass stars appear to be well-represented by a large virial parameter, requiring the presence of some additional factor such as external pressure to remain bound.

Some numerical simulations have also illustrated the importance of cloud pressure on the formation and evolution of dense cores. Lucas et al. (2017) show that for otherwise identical simulations of star-forming regions, the absence of a cloud envelope either at the beginning of formation, or the removal of such an envelope during evolution, leads to less dense substructure forming and to lower markedly star formation efficiencies.

Despite the differences in the analyses described above, it is striking that all of these studies come to a similar conclusion: pressure from the ambient cloud material on dense cores is important and often is required to keep the cores bound. The fact that this conclusion holds across such different star-forming environments from analyses using different techniques suggests that this phenomenon is a universal feature of star formation.

The one major component missing from most virial analyses of core populations is the support provided by magnetic fields. The magnetic field strength remains challenging to observe directly, although estimates can be made based on the field alignment, as measured by polarization data. Polarization observations are beginning to be available over larger areas of molecular clouds at lower resolution through telescopes such as Planck (e.g., Planck Collaboration et al. 2015) and Blast-Pol (e.g., Fissel et al. 2016), and at higher resolution with the JCMT's POL-2 (through the BISTRO survey; Ward-Thompson et al. 2017; Pattle et al. 2017).

5. CONCLUSION

We perform a simple virial analysis of the dense cores in Orion A and find that most of them are bound. We likely underestimate the true number that are bound, since our estimate of the binding pressure from the weight of filaments surrounding the dense cores is a lower limit to the true value. The majority of the dense core binding comes in the form of pressure, mostly from the weight of the ambient cloud material rather than self-gravity or other forms of binding pressure. Qualitatively, the picture that the pressure from surrounding molecular cloud material is important, or essential, to keeping dense cores bound appears common to a variety of local molecular cloud environments. Thanks to the efforts of a variety of recent surveys of nearby molecular clouds, there are high-quality, large-area maps available to allow for a uniform assessment of dense core sizes and masses (e.g., the JCMT and *Herschel* Gould Belt Surveys; Ward-Thompson et al. 2007b; André et al. 2010), dense core protostellar content (e.g., the *Spitzer* c2d and Gould Belt Surveys and the *Herschel* Gould Belt Survey Evans et al. 2009; Harvey et al. 2008; André et al. 2010), and ambient cloud material (e.g., using variants on the Near Infrared Colour Excess, or NICE technique; Lombardi & Alves 2001). The Green Bank Ammonia Survey (GAS; Friesen & Pineda et al. 2017) provides the necessary components to perform the type of virial analysis presented here, measuring both the temperatures and internal velocities of dense gas associated with the cores. The results of a similar virial analysis performed across all of the molecular clouds mapped by GAS should provide

an answer to the question of whether or not the pressure of molecular cloud material is indeed an essential component to (local) star formation.

APPENDIX

A. CORE CATALOGUES

Defining dense cores is generally challenging (e.g., Pineda et al. 2009) and is especially difficult in Orion A due to the high level of larger-scale structure present along the ISF. To test whether or not our conclusions are robust against uncertainties in the dense core definitions, we re-ran our analysis using two independently-derived core catalogues: the *FellWalker*-based catalogue from Lane et al. (2016) and a Hessian-based core identification algorithm presented and adopted in Salji et al. (2015). Both of these catalogues are based on the JCMT GBS SCUBA-2 850 μm data observations of Orion A, similar to the Lane et al. (2016) *getsources*-based catalogue used for our main analysis. Below, we describe each of these catalogues in detail and present a virial analysis based on each. We note that we do not include a similar analysis for the structure catalogues presented in Mairs et al. (2016), as that analysis does not extend far enough north in Orion A to match the GAS coverage.

A.1. *Lane et al. FellWalker Catalogue*

As discussed in Section 2.2, Lane et al. (2016) presented two dense core catalogues for Orion A, one using *getsources*, that we adopted for our main analysis, and also one using *FellWalker*, that we examine here. *FellWalker* identifies peaks based on local gradients, effectively associating any pixel lying along an upward path to a peak to that peak. There is no assumed shape for each core, and each pixel can be assigned to a maximum of one peak. When calculating the NH_3-based properties of each core, analagously to Section 2.4, we use the full core footprint. Otherwise, we follow an identical procedure to that presented for the *getsources*-based dense core catalogue.

In Figure 11, we show the results from the virial analysis using instead the *FellWalker* dense core catalogue. As in our main analysis, we see that nearly all of the dense cores are bound (energy density ratios greater than one). Only seven of the cores have sufficient self-gravity to be entirely bound without the pressure of the cloud (i.e., $-\Omega_G/\Omega_K \geq 2$), so our conclusion that pressure binding is required for the majority of dense cores holds.

A.2. *Salji et al. Catalogue*

Salji et al. (2015) analyzed the region around the ISF in Orion A using an early JCMT GBS data release that did not reach the final survey depth and an early reduction method which is less sensitive to larger-scale structure in the cloud ('Internal Release 1'). To identify dense cores, Salji et al. (2015) developed a new structure detection algorithm, tuned to identify only compact and roughly round sources. Sources identified with protostars were also removed from their final published catalogue. The remaining cores were classified as either starless or prestellar based on a thermal stability analysis using only SCUBA-2 data (and no kinematic information). To derive the NH_3-based properties for each core, we follow a similar procedure to that in the main analysis: we consider all pixels within the 1-σ contour of the peak core position. Since Salji et al. (2015) did not publish dense core axial ratios or a rotation angle, we assume the cores are well-described by a single radius.

The right panel of Figure 11 shows the virial analysis for the Salji et al. (2015) dense cores. Here, the cores appear to follow a much more linear trend, suggesting that higher self-gravity and higher

cloud pressure values tend to go together. The distinction that Salji et al. (2015) made between starless and prestellar cores does appear to be largely borne out in our virial analysis, with the prestellar cores tending to lie higher (more bound by both self-gravity and cloud pressure) than the starless cores. Although the qualitative appearance of the plot differs dramatically from our main analysis, we find that our main conclusion still holds: the majority of dense cores are bound (94%), and none would appear to be bound if the pressure from the cloud were ignored.

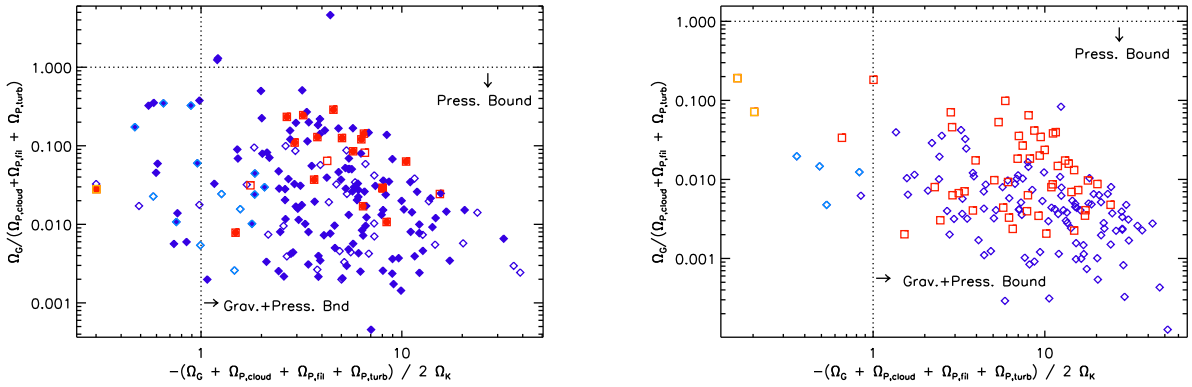

Figure 11. A comparison of the energy density ratio and confinement ratio for dense cores identified using *FellWalker* by Lane et al. (2016) (left panel) and by Salji et al. (2015) using a self-developed method (right panel). See Figure 6 for the plotting conventions used. Note that the right panel follows a different colour convention than previous figures: blue points show starless cores, while red points show prestellar cores. *Proto*stellar cores were eliminated from the Salji et al. (2015) catalogue and not published.

B. CLOUD PRESSURE ESTIMATE

As discussed in Section 2.5, one complication in estimating the external cloud pressure is determining whether gas on different scales is associated with the core or the cloud. Attributing *all* of the material observed to cloud-wide material would lead us to over-estimate the level of pressure exerted on the cores. In our main analysis, we filtered the Lombardi et al. (2014) column density map to trace only structures on ∼0.5 pc scales and larger. Here, we examine the impact of that choice of scale on our final results. We note that our test of the choice of scale also indirectly tests the choice in method for measuring the large-scale column density. The variations between methods at a single spatial scale is likely to be much smaller than the variation induced by significant changes to the scale adopted.

The *a Trous* algorithm we apply for filtering can be applied on length scales of 2^N pixels. For context, 0.48 pc corresponds to 16 pixels in the original Lombardi et al. (2014) map. In Figure 12, we show a comparable analysis to that in Figure 8 but with the cloud pressure calculated instead from a column density map filtered to 0.24 pc (8 pixels) and 0.97 pc (32 pixels). Although points do shift for each of the different column density choices, minimal changes to the energy density ratio distribution above or below one occur.

In Figure 13, we examine the most extreme cases, comparing the results if instead the full, unfiltered column density map or an extremely filtered map (7.7 pc or 256 pixels) were used. In the case of no filtering, we again see that most of the cores have energy density ratios above one. Only

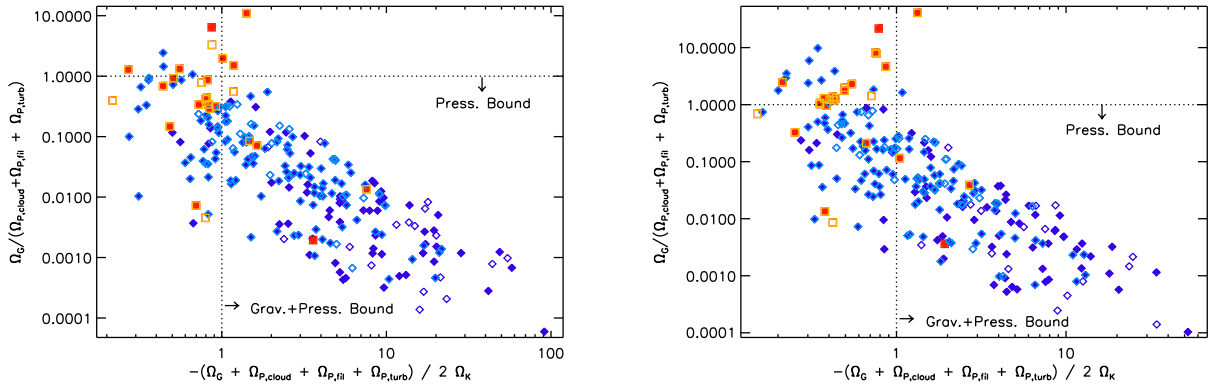

Figure 12. Examining the effect of different smoothing scales on the cloud pressure derived for each core. The left panel shows the cloud pressure derived including the cloud column density up to scales a factor of two smaller than the nominal value (i.e., roughly 0.25 pc). The right panel shows the cloud pressure derived including the cloud column density up to scales a factor of two larger than the nominal value (i.e., 1 pc). There is only a minimal shift in the points compared to Figure 8; in both cases, nearly all cores remain sub-virial and pressure-bound. See Figure 6 for the plotting conventions used.

in the extremely filtered map, do we find that the majority of cores are unbound. In other words, a significant amount of cloud material must be excluded from our cloud pressure estimate for most of the dense cores to be not pressure-confined.

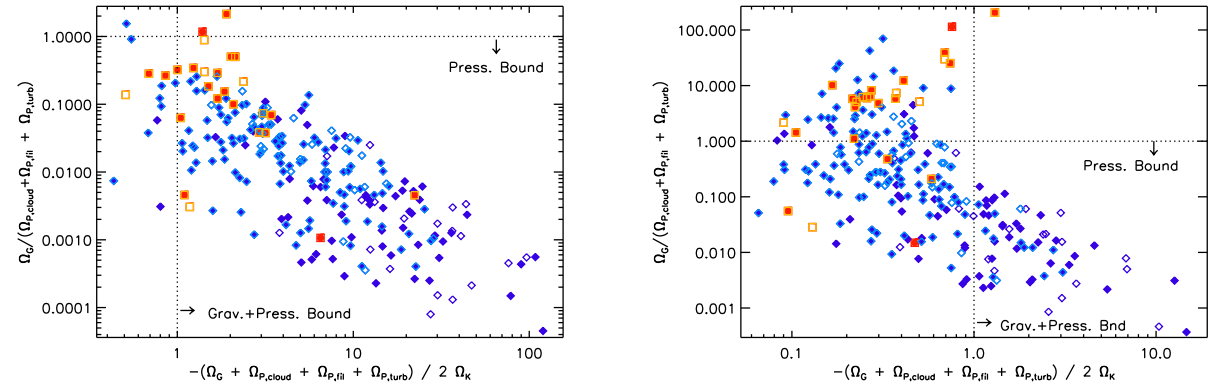

Figure 13. Examining the effect of different smoothing scales on the cloud pressure derived for each core. The left panel shows the cloud pressure derived using the total cloud column density measured, i.e., with no filtering applied. The right panel shows the cloud pressure derived including only the maximum smoothing scale for the cloud column density, i.e., 8 pc. In the former case, nearly all dense cores are sub-virial and pressure-bound, while in the latter case, many of the cores are super-virial, while pressure continues to dominate over gravity regardless of the level of confinement on the core. See Figure 6 for the plotting conventions used.

These tests show that barring an extreme allocation of core-like and cloud-like material in the Lombardi et al. (2014) extinction map, we come to the same conclusion: pressure from the ambient cloud material strongly dominates over self-gravity in keeping the dense cores bound. Given the fact that the amount of cloud pressure estimated for each core varies by a significant amount (often a

factor of 10 between the non-filtered and maximally-filtered cases), we may also surmise that changing the overarching assumption in our method, i.e., assuming that the cloud is spherically symmetric, is also unlikely to change this conclusion, although the precise amount of pressure-binding attributable to each core would vary under different models.

C. CLOUD PRESSURE DERIVATION

Here we derive a useful expression for the hydrostatic pressure on a protostellar core embedded within a larger cloud. We begin with a spherical cloud of radius $R_{\rm cl}$, with a density profile $\rho(r)$, enclosed mass $m(r) = \int_0^r 4\pi\rho(r')r'^2\,dr'$, and mean column (or more precisely, mass surface density) $\bar{\Sigma}(r) = m(r)/(\pi r^2)$ within r. The bounding pressure is $P(R_{\rm cl}) = P_s$. From any point, the column to the surface (along a radial path) is $\Sigma_s(r) = \int_r^{R_{\rm cl}} \rho(r')\,dr'$. The wisdom of these definitions is that the hydrostatic relation can be rewritten entirely in terms of column density:

$$dP = -\frac{Gm\rho}{r^2}\,dr = \pi G\bar{\Sigma}\,d\Sigma_s, \tag{C1}$$

which can be integrated if the relation between $\bar{\Sigma}$ and Σ_s is known. Note also that

$$d\Sigma_s = -\rho\,dr = -\frac{dm}{4\pi r^2} = -d\frac{m}{4\pi r^2} - \frac{m}{2\pi r^3}dr = -\frac{d\bar{\Sigma}}{4} - \frac{\bar{\Sigma}}{2}\frac{dr}{r}.$$

Suppose we adopt a power-law density profile, $\rho \propto r^{-k}$, for which $\bar{\Sigma} \propto r^{1-k}$; then $4(k-1)d\Sigma_s = (3-k)d\bar{\Sigma}$. If $\bar{\Sigma}_{\rm cl} = \bar{\Sigma}(R_{\rm cl})$ is the mean column of the entire cloud,

$$\bar{\Sigma} = \bar{\Sigma}_{\rm cl} + \frac{4(k-1)}{3-k}\Sigma_s.$$

Equation (C1) can then be integrated:

$$P(r) - P_s = \pi G\bar{\Sigma}_{\rm cl}\Sigma_s + \frac{2(k-1)}{3-k}\pi G\Sigma_s^2. \tag{C2}$$

The pressure is related to the mean cloud column and the column to the surface; for the characteristic GMC profile $k = 1$, equation (C2) reduces to the expression given by McKee (1989).

Within our power-law density profile, one could also use the expression $P(r) = (R_{\rm cl}/r)^{k_P}\,P_s$ where $k_P = 2(k-1)$ (McKee & Tan 2003). The advantage of expression (C2) is that it avoids making reference to the radius r, and is therefore more closely related to observed quantities and more robust to deviations from spherical symmetry.

It is also useful to consider non-spherical geometries like sheets and cylinders, for which the maximum column $\Sigma_\perp$ perpendicular to the axis (for cylinders) or along the surface normal (for sheets) is the relevant scale; this quantity is twice the maximum value of Σ_s. For a sheet confined by a surface pressure P_s, the overpressure is $P(\Sigma_s) - P_s = 2\pi G\Sigma_s(\Sigma_\perp - \Sigma_s)$, for which the maximum (midplane) value is $(\pi/2)G\Sigma_\perp^2$. Within an unmagnetized isothermal filament (Stodólkiewicz 1963; Ostriker 1964), the central pressure is at least[6] $(2/\pi)G\Sigma_\perp^2$.

When estimating the pressure on a given core, one generally does not know the values of Σ_s and $\bar{\Sigma}_{\rm cl}$ directly from observations, but rather the projected column $\Sigma(x, y)$ without any indication how much column is in the background. For this reason, we now consider how P should be inferred from the column map.

[6] In our expression $\Sigma_\perp$ neglects the column of the bounding medium, and P reaches this lower limit when the bounding pressure is effectively zero.

C.1. *Evaluation for an observed core*

What is the most reasonable range of pressures to associate with a specific core, given a map of the projected column Σ? A natural choice is to associate $\bar{\Sigma}_{\rm cl}$ with the mean of Σ within the cloud boundaries, and Σ_s with one-half of Σ at the location in question, but there are several ambiguities. First, the external pressure P_s must be guessed at. Second, our Σ map may be contaminated by emission unrelated to the structure of interest. Third, if the density distribution is not isotropic, Σ is affected by inclination. Fourth, one usually does not know how much of Σ is in front of the core and hence what value to associate with Σ_s/Σ. Finally, observations may suffer from intrinsic uncertainties involving finite resolution, spatial filtering, emission-to-mass conversions, and the like.

We concentrate on the fourth ambiguity (foreground and background). The natural assumption that half of Σ is in the foreground tends to maximize P, but it is more rigorous to adopt a model and some prior expectations regarding the occurrence of cores within clouds, and derive a probability distribution from P. Let us assume: (*i*) No cores exist with $\Sigma_s < \Sigma_{s,\rm min}$, a situation corresponding to extinction thresholds observed in various regions (Pak et al. 1998; Johnstone et al. 2004) perhaps because of FUV photo-ionization (McKee 1989). (*ii*) The probability of finding a core scales as ρ^α per unit volume, a scenario accommodating a constant star formation rate per unit mass ($\alpha = 1$) and a dynamically-limited rate ($\alpha = 2$).

The differential cumulative probability is then $d\mathscr{P} \propto \rho^\alpha dz$, where z is distance along the line of sight, except $d\mathscr{P} = 0$ where $P < P(\Sigma_{s,\rm min})$.

For the special case $\alpha = 1$, $d\mathscr{P} \propto d\Sigma$ so the column toward the core is uniformly distributed within its allowed range. In the case of a planar sheet, Σ_s is uniformly distributed from $\Sigma_{s,\rm min}$ to $\Sigma_\perp/2$. The median pressure within this distribution is lower than the midplane value by $(\pi/2)G(\Sigma_\perp/2-\Sigma_{s,\rm min})^2$.

To go further, we require relations among P, ρ, and z. Hence, we adopt here the spherical model: then $P \propto \rho^{\gamma_p}$ where $\gamma_p = k_P/k = 2-2/k$ is the polytropic exponent. Also, $P \propto r^{-k_P} \propto (z^2+\varpi^2)^{-k_P/2}$ if ϖ is the projected offset from the cloud center and $z = 0$ at the cloud center. Working out dz in terms of dP,

$$d\mathscr{P} \propto \frac{P^{(\alpha/2-1)k/(k-1)}}{|z(P)|}\,dP \propto \frac{P^{(\alpha/2-1)k/(k-1)}}{\left[(P/\max P)^{-2/k_P}-1\right]^{1/2}}\,dP. \tag{C3}$$

Note that for the dynamical star formation rate ($\alpha = 2$) the numerator is constant and $d\mathscr{P} \propto |z(P)|^{-1}\,dP$ so long as $k \neq 1$.

The next step is to determine the maximum possible pressure by determining the maximum value of Σ_s along the line of sight, given the observed value of Σ, i.e., $\max P = P(\max \Sigma_s)$. Often we can ignore the cloud boundary and extend a line-of-sight integration to infinity. This assumption is especially reasonable if $P(\Sigma_{s,\rm min}) \gg P_s$, which is usually the case for giant molecular clouds. We then obtain

$$\frac{\Sigma}{\max \Sigma_s} = \pi^{1/2}(k-1)\frac{\Gamma[(k-1)/2]}{\Gamma(k/2)} \simeq k+1+(\pi-3)(k-1)(3-k). \tag{C4}$$

The middle expression comes from integrating through an infinite sphere, and the quadratic approximation is exact for $k = 1, 2, 3$ and errs by only 0.6% over the entire range. It shows that the usual assumption ($\max \Sigma_s = \Sigma/2$) is correct when $k = 1$, but amounts to an over-prediction in steeper density profiles.

Once $\max \Sigma_s$ and $\max P$ have been determined, equation (C3) provides the probability density. In Figure 14, we plot the factor relating the median over-pressure to the maximum value.

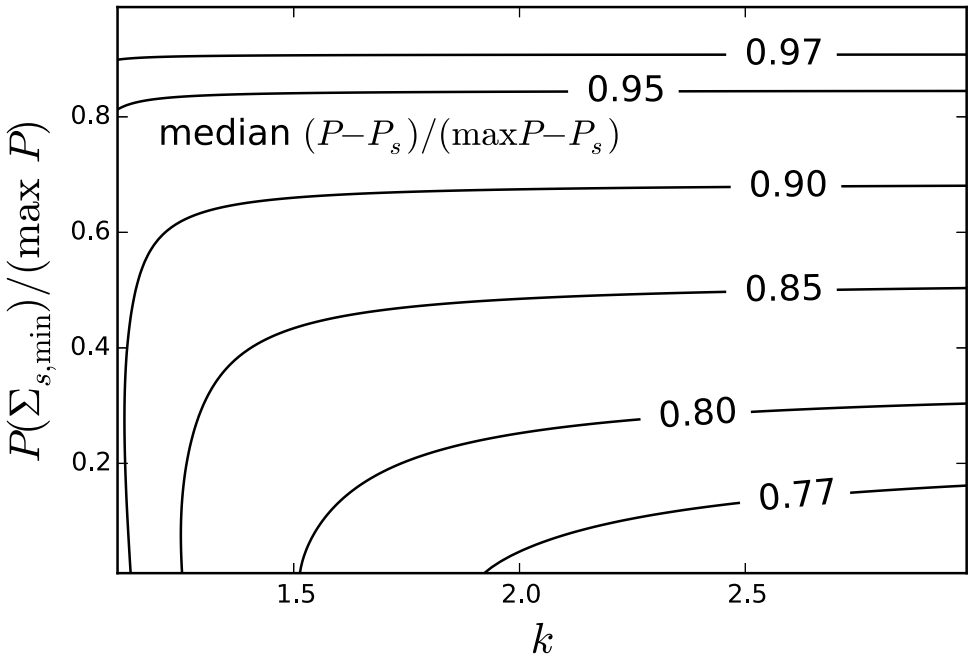

Figure 14. Median over-pressure, relative to the theoretical maximum, for cores detected within spherical clouds, assuming the probability per unit volume scales as ρ^2 for columns $\Sigma_s > \Sigma_{s,\min}$ to the surface, i.e. pressures $P > P(\Sigma_{s,\min})$. Theoretical maximum and minimum pressures are determined from $\Sigma_{s,\min}$ and $\max \Sigma_s$ (eq. C4) via equation (C2), and the probability density follows equation (C3). This plot assumes $P(\Sigma_{s,\min}) \ll P(\Sigma/2)$.

RKF is a Dunlap Fellow at the Dunlap Institute for Astronomy & Astrophysics. The Dunlap Institute is funded through an endowment established by the David Dunlap family and the University of Toronto. JEP, PC, ACT, and AP acknowledge the financial support of the European Research Council (ERC; project PALs 320620). EWR and CDM are supported by Discovery Grants from NSERC of Canada. The National Radio Astronomy Observatory is a facility of the National Science Foundation operated under cooperative agreement by Associated Universities, Inc. SSRO is supported by NSF grant AST-1510021. The JCMT has historically been operated by the Joint Astronomy Centre on behalf of the Science and Technology Facilities Council of the United Kingdom, the National Research Council of Canada and the Netherlands Organisation for Scientific Research. Additional funds for the construction of SCUBA-2 were provided by the Canada Foundation for Innovation. The identification number for the programme under which the SCUBA-2 data used in this paper is MJLSG41. This research made use of Astropy, a community-developed core Python package for Astronomy (Astropy Collaboration et al. 2013). Figures in this paper were creating using the NASA IDL astronomy library (Landsman 1993) and the Coyote IDL library (`http://www.idlcoyote.com/index.html`)

Facility: Green Bank Telescope, JCMT (SCUBA-2)

Software: Astropy (Astropy Collaboration et al. 2013), Starlink(Currie et al. 2014), atrous.pro (`https://github.com/low-sky/idl-low-sky/tree/master/wavelet`)

REFERENCES

Alves, F. O., Franco, G. A. P., & Girart, J. M. 2008, A&A, 486, L13

Alves, J., Lombardi, M., & Lada, C. J. 2007, A&A, 462, L17

André, P., Di Francesco, J., Ward-Thompson, D., et al. 2014, Protostars and Planets VI, 27

André, P., Men'shchikov, A., Bontemps, S., et al. 2010, A&A, 518, L102

Arzoumanian, D., André, P., Didelon, P., et al. 2011, A&A, 529, L6

Astropy Collaboration, Robitaille, T. P., Tollerud, E. J., et al. 2013, A&A, 558, A33

Bailey, N. D., Basu, S., & Caselli, P. 2015, ApJ, 798, 75

Ballesteros-Paredes, J., Gómez, G. C., Pichardo, B., & Vázquez-Semadeni, E. 2009, MNRAS, 393, 1563

Ballesteros-Paredes, J., Klessen, R. S., & Vázquez-Semadeni, E. 2003, ApJ, 592, 188

Bally, J. 2008, Overview of the Orion Complex, ed. B. Reipurth, 459

Barnes, P. J., Hernandez, A. K., O'Dougherty, S. N., Schap, III, W. J., & Muller, E. 2016, ApJ, 831, 67

Beaumont, C. N., Offner, S. S. R., Shetty, R., Glover, S. C. O., & Goodman, A. A. 2013, ApJ, 777, 173

Bergin, E. A., & Tafalla, M. 2007, ARA&A, 45, 339

Berry, D. S. 2015, Astronomy and Computing, 10, 22

Bertoldi, F., & McKee, C. F. 1992, ApJ, 395, 140

Bonnor, W. B. 1956, MNRAS, 116, 351

Caselli, P., & Myers, P. C. 1995, ApJ, 446, 665

Caselli, P., Walmsley, C. M., Zucconi, A., et al. 2002, ApJ, 565, 331

Caselli, P., Bizzocchi, L., Keto, E., et al. 2017, ArXiv e-prints

Chandrasekhar, S., & Fermi, E. 1953, ApJ, 118, 116

Crapsi, A., Caselli, P., Walmsley, M. C., & Tafalla, M. 2007, A&A, 470, 221

Currie, M. J., Berry, D. S., Jenness, T., et al. 2014, in Astronomical Society of the Pacific Conference Series, Vol. 485, Astronomical Data Analysis Software and Systems XXIII, ed. N. Manset & P. Forshay, 391

Dempsey, J. T., Friberg, P., Jenness, T., et al. 2013, MNRAS, 430, 2534

Di Francesco, J., Evans, II, N. J., Caselli, P., et al. 2007, Protostars and Planets V, 17

Ebert, R. 1955, ZA, 37, 217

Elmegreen, B. G. 1989, ApJ, 338, 178

Evans, II, N. J., Dunham, M. M., Jørgensen, J. K., et al. 2009, ApJS, 181, 321

Field, G. B., Blackman, E. G., & Keto, E. R. 2011, MNRAS, 416, 710

Fissel, L. M., Ade, P. A. R., Angilè, F. E., et al. 2016, ApJ, 824, 134

Foster, J. B., Rosolowsky, E. W., Kauffmann, J., et al. 2009, ApJ, 696, 298

Friesen, R. K., Pineda, J. E., Rosolowsky, E., et al. 2017, ArXiv e-prints

Gaches, B. A. L., Offner, S. S. R., Rosolowsky, E. W., & Bisbas, T. G. 2015, ApJ, 799, 235

Gong, M., & Ostriker, E. C. 2015, ApJ, 806, 31

Goodman, A. A., Barranco, J. A., Wilner, D. J., & Heyer, M. H. 1998, ApJ, 504, 223

Hartmann, L. 1998, Accretion Processes in Star Formation

Harvey, P. M., Huard, T. L., Jørgensen, J. K., et al. 2008, ApJ, 680, 495

Henshaw, J. D., Caselli, P., Fontani, F., et al. 2013, MNRAS, 428, 3425

Hillenbrand, L. A. 1997, AJ, 113, 1733

Ikeda, N., & Kitamura, Y. 2009, ApJL, 705, L95

Ikeda, N., Sunada, K., & Kitamura, Y. 2007, ApJ, 665, 1194

Jijina, J., Myers, P. C., & Adams, F. C. 1999, ApJS, 125, 161

Johnstone, D., & Bally, J. 1999, ApJL, 510, L49

Johnstone, D., Di Francesco, J., & Kirk, H. 2004, ApJL, 611, L45

Johnstone, D., Fich, M., Mitchell, G. F., & Moriarty-Schieven, G. 2001, ApJ, 559, 307

Johnstone, D., Wilson, C. D., Moriarty-Schieven, G., et al. 2000, ApJ, 545, 327
Kainulainen, J., Federrath, C., & Henning, T. 2014, Science, 344, 183
Kauffmann, J., Bertoldi, F., Bourke, T. L., Evans, II, N. J., & Lee, C. W. 2008, A&A, 487, 993
Kauffmann, J., Pillai, T., & Goldsmith, P. F. 2013, ApJ, 779, 185
Keto, E. R., & Myers, P. C. 1986, ApJ, 304, 466
Kim, M. K., Hirota, T., Honma, M., et al. 2008, PASJ, 60, 991
Kirk, H., Johnstone, D., & Di Francesco, J. 2006, ApJ, 646, 1009
Kirk, H., Johnstone, D., & Tafalla, M. 2007, ApJ, 668, 1042
Kirk, H., Di Francesco, J., Johnstone, D., et al. 2016, ApJ, 817, 167
Kirk, J. M., Ward-Thompson, D., Palmeirim, P., et al. 2013, MNRAS, 432, 1424
Lada, C. J., Muench, A. A., Rathborne, J., Alves, J. F., & Lombardi, M. 2008, ApJ, 672, 410
Landsman, W. B. 1993, in Astronomical Society of the Pacific Conference Series, Vol. 52, Astronomical Data Analysis Software and Systems II, ed. R. J. Hanisch, R. J. V. Brissenden, & J. Barnes, 246
Lane, J., Kirk, H., Johnstone, D., et al. 2016, ApJ, 833, 44
Larson, R. B. 1981, MNRAS, 194, 809
Li, D., Kauffmann, J., Zhang, Q., & Chen, W. 2013, ApJL, 768, L5
Li, D., Velusamy, T., Goldsmith, P. F., & Langer, W. D. 2007, ApJ, 655, 351
Lombardi, M., & Alves, J. 2001, A&A, 377, 1023
Lombardi, M., Bouy, H., Alves, J., & Lada, C. J. 2014, A&A, 566, A45
Lucas, W. E., Bonnell, I. A., & Forgan, D. H. 2017, MNRAS
Mairs, S., Johnstone, D., Kirk, H., et al. 2016, MNRAS, 461, 4022
Maruta, H., Nakamura, F., Nishi, R., Ikeda, N., & Kitamura, Y. 2010, ApJ, 714, 680
McKee, C. F. 1989, ApJ, 345, 782
McKee, C. F., & Tan, J. C. 2003, ApJ, 585, 850
Megeath, S. T., Gutermuth, R., Muzerolle, J., et al. 2012, AJ, 144, 192
Meingast, S., Alves, J., Mardones, D., et al. 2016, A&A, 587, A153
Men'shchikov, A., André, P., Didelon, P., et al. 2012, A&A, 542, A81
Menten, K. M., Reid, M. J., Forbrich, J., & Brunthaler, A. 2007, A&A, 474, 515
Mezger, P. G., Zylka, R., & Wink, J. E. 1990, A&A, 228, 95
Miettinen, O., Harju, J., Haikala, L. K., & Juvela, M. 2010, A&A, 524, A91
Myers, P. C. 2005, ApJ, 623, 280
Naranjo-Romero, R., Vázquez-Semadeni, E., & Loughnane, R. M. 2015, ApJ, 814, 48
Nutter, D., & Ward-Thompson, D. 2007, MNRAS, 374, 1413
Ossenkopf, V., & Henning, T. 1994, A&A, 291, 943
Ostriker, J. 1964, ApJ, 140, 1056
Pak, S., Jaffe, D. T., van Dishoeck, E. F., Johansson, L. E. B., & Booth, R. S. 1998, ApJ, 498, 735
Pattle, K. 2016, MNRAS, 459, 2651
Pattle, K., Ward-Thompson, D., Kirk, J. M., et al. 2015, MNRAS, 450, 1094
—. 2016, ArXiv e-prints
Pattle, K., Ward-Thompson, D., Berry, D., et al. 2017, ArXiv e-prints
Pineda, J. E., Goodman, A. A., Arce, H. G., et al. 2010, ApJL, 712, L116
Pineda, J. E., Rosolowsky, E. W., & Goodman, A. A. 2009, ApJL, 699, L134
Planck Collaboration, Ade, P. A. R., Aghanim, N., et al. 2015, A&A, 576, A104
Polychroni, D., Schisano, E., Elia, D., et al. 2013, ApJL, 777, L33
Sadavoy, S. I., Shirley, Y., Di Francesco, J., et al. 2015, ApJ, 806, 38
Sadavoy, S. I., Di Francesco, J., Bontemps, S., et al. 2010, ApJ, 710, 1247
Salji, C. J., Richer, J. S., Buckle, J. V., et al. 2015, MNRAS, 449, 1769
Seo, Y. M., & Youdin, A. N. 2016, MNRAS, 461, 1088
Seo, Y. M., Shirley, Y. L., Goldsmith, P., et al. 2015, ApJ, 805, 185
Shimajiri, Y., Kawabe, R., Takakuwa, S., et al. 2011, PASJ, 63, 105
Shimajiri, Y., Kitamura, Y., Saito, M., et al. 2014, A&A, 564, A68
Shirley, Y. L. 2015, PASP, 127, 299
Sohn, J., Lee, C. W., Park, Y.-S., et al. 2007, ApJ, 664, 928
Steinacker, J., Baes, M., & Gordon, K. D. 2013, ARA&A, 51, 63

Stodólkiewicz, J. S. 1963, AcA, 13, 30

Stutz, A. M., Tobin, J. J., Stanke, T., et al. 2013, ApJ, 767, 36

Tafalla, M., & Hacar, A. 2015, A&A, 574, A104

Tafalla, M., Myers, P. C., Caselli, P., Walmsley, C. M., & Comito, C. 2002, ApJ, 569, 815

Tatematsu, K., Kandori, R., Umemoto, T., & Sekimoto, Y. 2008, PASJ, 60, 407

van Kempen, T. A., van Dishoeck, E. F., Salter, D. M., et al. 2009, A&A, 498, 167

Ward-Thompson, D., André, P., Crutcher, R., et al. 2007a, Protostars and Planets V, 33

Ward-Thompson, D., Di Francesco, J., Hatchell, J., et al. 2007b, PASP, 119, 855

Ward-Thompson, D., Pattle, K., Bastien, P., et al. 2017, ArXiv e-prints

Whitworth, A. P., & Ward-Thompson, D. 2001, ApJ, 547, 317

Table 1. Dense Core Properties

ID[a]	R.A.[a]	Decl.[a]	M[a]	R_{eff}[a]	C[a]	Pr?[a]	σ_{obs} (km/s)[b]			T_{kin}(K)[b]			$\log(P_c/k_B)$[c]	Vir.[d]	$-\Omega_G/\Omega_K$[d]	$\Omega_G/\Omega_{P,c}$[d]
	(J2000)	(J2000)	($M_\odot$)	(pc)			mn	err	std	mn	err	std	$\log(K/cm^3)$	Rat.		
5	83.84726	-5.02459	8.28	0.017	0.64	Y	0.311	0.002	0.041	17.5	0.1	0.8	7.3	1.4E+00	2.6E+00	2.0E+01
9	83.86135	-5.16620	11.10	0.023	0.48	Y	0.435	0.001	0.067	23.3	0.1	1.5	7.3	8.2E-01	1.5E+00	1.1E+01
10	83.82113	-5.32181	4.92	0.017	0.51	N	0.542	0.001	0.075	25.2	0.0	0.8	7.5	3.9E-01	6.2E-01	4.2E+00
12	83.81898	-5.32483	3.84	0.017	0.58	N	0.517	0.001	0.084	25.5	0.0	1.0	7.5	3.7E-01	5.2E-01	2.5E+00
16	83.81604	-5.33532	2.06	0.025	0.69	N	0.477	0.001	0.084	28.1	0.0	1.5	7.5	8.5E-01	2.1E-01	1.4E-01
17	83.82469	-5.31807	2.93	0.017	0.54	N	0.563	0.001	0.064	25.2	0.0	0.9	7.5	2.9E-01	3.5E-01	1.6E+00
18	83.81026	-5.31189	3.64	0.026	0.62	N	0.450	0.001	0.109	23.7	0.0	0.8	7.4	6.1E-01	4.1E-01	5.0E-01
19	83.86445	-5.15861	3.11	0.027	0.63	Y	0.423	0.001	0.074	23.7	0.1	1.7	7.3	5.8E-01	3.8E-01	4.8E-01
21	83.84284	-5.01978	3.61	0.017	0.56	Y	0.272	0.001	0.052	17.0	0.1	0.7	7.3	8.5E-01	1.3E+00	3.7E+00
23	83.82478	-5.00483	2.49	0.017	0.62	N	0.341	0.001	0.033	17.8	0.0	0.4	7.2	5.2E-01	6.9E-01	1.9E+00
30	83.83122	-5.25931	1.82	0.018	0.60	Y	0.329	0.001	0.032	19.9	0.1	0.7	7.2	4.9E-01	4.9E-01	1.0E+00
32	83.82470	-5.31361	2.94	0.018	0.39	N	0.565	0.001	0.071	25.1	0.0	1.0	7.4	2.9E-01	3.3E-01	1.4E+00
33	83.85801	-5.09514	2.92	0.017	0.54	Y	0.212	0.000	0.031	17.0	0.0	0.9	7.3	1.0E+00	1.4E+00	2.3E+00
34	83.83522	-5.01365	4.37	0.027	0.58	N	0.290	0.001	0.060	17.2	0.0	0.6	7.3	1.0E+00	9.5E-01	8.9E-01
35	83.85934	-5.06551	2.03	0.017	0.58	Y	0.275	0.002	0.096	16.4	0.1	0.9	7.3	7.1E-01	7.6E-01	1.2E+00
36	83.87365	-4.97983	1.84	0.017	0.56	Y	0.478	0.003	0.131	18.6	0.1	1.5	7.1	2.5E-01	3.0E-01	1.6E+00
39	83.85962	-5.17263	2.08	0.017	0.51	N	0.401	0.001	0.083	22.6	0.1	1.5	7.3	3.8E-01	4.3E-01	1.2E+00
40	83.86029	-5.08760	3.89	0.026	0.57	N	0.202	0.000	0.013	16.5	0.0	0.5	7.3	1.5E+00	1.3E+00	8.3E-01
41	83.78702	-5.93102	3.25	0.017	0.50	Y	0.264	0.001	0.092	14.6	0.1	0.8	7.0	8.0E-01	1.3E+00	5.1E+00
42	83.84709	-5.20066	1.48	0.017	0.58	Y	0.301	0.000	0.073	19.4	0.0	0.4	7.2	5.7E-01	4.7E-01	6.9E-01
43	83.78889	-5.33678	2.93	0.029	0.51	N	0.357	0.001	0.086	22.6	0.1	0.9	7.5	1.3E+00	4.1E-01	1.8E-01
44	83.82886	-5.01357	1.41	0.017	0.64	Y	0.311	0.001	0.064	17.5	0.0	0.7	7.2	5.9E-01	4.4E-01	6.0E-01
47	83.85118	-5.14224	1.40	0.017	0.62	Y	0.346	0.001	0.080	19.7	0.1	0.5	7.3	5.3E-01	3.7E-01	5.3E-01

Table 1 continued on next page

Table 1 *(continued)*

ID[a]	R.A.[a]	Decl.[a]	M[a]	R_{eff}[a]	C[a]	Pr?[a]	σ_{obs} (km/s)[b]			T_{kin}(K)[b]			$\log(P_c/k_B)$[c]	Vir.[d]	$-\Omega_G/\Omega_K$[d]	$\Omega_G/\Omega_{P,c}$[d]
	(J2000)	(J2000)	($M_\odot$)	(pc)			mn	err	std	mn	err	std	log(K/cm^3)	Rat.		
49	83.83959	-5.21998	2.99	0.027	0.59	N	0.342	0.001	0.055	19.8	0.0	0.9	7.2	7.6E-01	5.0E-01	4.9E-01
50	83.85229	-5.13106	2.22	0.017	0.51	N	0.374	0.001	0.045	19.5	0.0	0.7	7.3	4.6E-01	5.3E-01	1.3E+00
54	83.80960	-5.30330	1.91	0.022	0.52	N	0.423	0.001	0.077	23.3	0.0	0.6	7.4	6.2E-01	2.8E-01	3.0E-01
55	83.83234	-5.21963	1.10	0.023	0.64	N	0.298	0.001	0.062	19.3	0.0	1.1	7.2	1.0E+00	2.7E-01	1.5E-01
56	83.82595	-5.00943	1.44	0.017	0.59	Y	0.327	0.001	0.051	17.7	0.0	0.6	7.2	5.4E-01	4.2E-01	6.3E-01
57	83.87378	-4.99644	0.69	0.017	0.61	Y	0.453	0.004	0.193	18.5	0.2	1.5	7.1	3.9E-01	1.2E-01	1.9E-01
58	83.84570	-5.21045	6.84	0.041	0.50	N	0.347	0.000	0.049	19.7	0.0	0.5	7.2	1.1E+00	7.6E-01	5.1E-01
59	83.80631	-5.96555	1.74	0.018	0.58	Y	0.271	0.002	0.054	15.1	0.1	1.0	7.1	6.1E-01	6.6E-01	1.2E+00
63	83.74833	-5.35940	2.05	0.026	0.44	N	0.552	0.004	0.087	21.4	0.2	1.2	7.2	4.1E-01	1.7E-01	2.7E-01
65	83.80722	-5.44595	7.74	0.054	0.40	N	0.689	0.003	0.112	27.3	0.1	2.9	7.3	7.0E-01	2.1E-01	1.7E-01
68	83.86681	-5.17436	1.04	0.018	0.54	N	0.369	0.001	0.091	22.1	0.1	1.5	7.3	5.5E-01	2.3E-01	2.6E-01
69	83.85507	-5.04317	1.04	0.029	0.73	N	0.215	0.001	0.040	16.4	0.1	0.8	7.3	4.3E+00	3.0E-01	3.7E-02
70	83.73424	-5.76767	2.92	0.023	0.43	N	0.586	0.002	0.088	15.9	0.1	0.8	7.1	2.5E-01	2.6E-01	1.0E+00
72	83.81564	-4.99858	1.11	0.022	0.60	N	0.324	0.001	0.049	18.0	0.1	0.8	7.2	9.2E-01	2.6E-01	1.6E-01
73	83.78455	-5.59903	1.90	0.021	0.49	Y	0.318	0.001	0.037	15.9	0.1	0.7	7.1	5.7E-01	4.9E-01	7.6E-01
77	83.77707	-4.91264	0.68	0.017	0.58	N	0.224	0.001	0.052	18.7	0.1	1.1	6.8	5.8E-01	3.0E-01	3.5E-01
81	83.67071	-5.52846	1.42	0.017	0.56	Y	0.250	0.005	0.039	14.3	0.6	1.1	6.7	4.8E-01	6.3E-01	2.0E+00
82	83.84701	-5.12541	2.39	0.025	0.51	N	0.374	0.001	0.043	19.3	0.0	0.8	7.3	7.6E-01	3.9E-01	3.4E-01
83	83.77700	-4.94065	1.83	0.023	0.48	N	0.221	0.001	0.039	17.7	0.1	0.9	7.0	8.4E-01	6.2E-01	5.9E-01
84	83.83829	-5.24769	1.59	0.030	0.58	N	0.239	0.001	0.036	19.6	0.1	0.5	7.2	1.9E+00	3.7E-01	1.1E-01
91	83.77017	-5.40508	1.25	0.025	0.48	N	0.639	0.010	0.077	23.6	0.4	2.2	7.4	5.6E-01	8.4E-02	8.1E-02
93	83.78789	-5.97440	1.34	0.017	0.53	Y	0.181	0.001	0.026	14.0	0.1	0.7	7.0	9.1E-01	8.4E-01	8.6E-01
95	83.80558	-4.99034	0.49	0.025	0.73	N	0.295	0.002	0.066	17.8	0.1	1.7	7.2	2.8E+00	1.1E-01	2.0E-02
97	83.77125	-5.62290	1.08	0.026	0.65	N	0.267	0.001	0.047	15.0	0.1	0.6	7.1	1.6E+00	2.9E-01	1.0E-01
99	84.04762	-6.17912	1.92	0.026	0.62	N	0.266	0.001	0.041	13.3	0.1	0.6	6.9	8.0E-01	5.4E-01	5.1E-01

Table 1 continued on next page

Table 1 *(continued)*

ID[a]	R.A.[a]	Decl.[a]	M[a]	R_{eff}[a]	C[a]	Pr?[a]	σ_{obs} (km/s)[b]			T_{kin}(K)[b]			$\log(P_c/k_B)$[c]	Vir.[d]	$-\Omega_G/\Omega_K$[d]	$\Omega_G/\Omega_{P,c}$[d]
	(J2000)	(J2000)	($M_\odot$)	(pc)			mn	err	std	mn	err	std	log(K/cm^3)	Rat.		
100	83.85114	-5.20867	1.68	0.023	0.58	N	0.355	0.000	0.046	19.6	0.0	0.5	7.2	7.1E-01	3.2E-01	2.9E-01
101	83.86029	-5.10059	2.45	0.031	0.51	N	0.235	0.001	0.044	17.6	0.0	1.0	7.3	2.1E+00	5.9E-01	1.6E-01
105	83.84746	-5.11968	2.03	0.025	0.40	N	0.377	0.001	0.034	19.1	0.1	0.7	7.3	7.8E-01	3.3E-01	2.7E-01
107	83.76559	-5.30012	0.73	0.018	0.54	N	0.187	0.004	0.091	16.7	0.4	1.9	7.1	1.2E+00	4.0E-01	1.9E-01
108	83.84002	-5.24101	2.25	0.032	0.50	N	0.224	0.001	0.022	19.7	0.1	0.7	7.2	1.9E+00	5.2E-01	1.6E-01
109	83.84306	-5.17037	0.66	0.017	0.51	N	0.194	0.001	0.036	19.0	0.1	1.1	7.3	1.5E+00	3.3E-01	1.3E-01
110	83.88081	-5.01031	0.52	0.018	0.55	N	0.298	0.006	0.220	19.9	0.6	2.1	7.1	9.0E-01	1.6E-01	9.9E-02
114	83.80598	-5.45109	1.91	0.029	0.55	N	0.660	0.004	0.098	25.6	0.2	3.2	7.2	4.1E-01	1.0E-01	1.5E-01
116	83.85353	-5.13791	1.03	0.018	0.55	N	0.360	0.001	0.067	19.8	0.0	0.6	7.3	6.4E-01	2.4E-01	2.3E-01
117	83.70287	-4.92851	0.60	0.020	0.60	N	0.214	0.009	0.053	20.4	0.9	2.9	6.7	6.7E-01	2.3E-01	2.0E-01
121	83.96774	-6.16719	0.87	0.017	0.56	Y	0.536	0.007	0.101	14.7	0.3	1.9	6.9	1.8E-01	1.2E-01	5.3E-01
122	83.77141	-5.57990	1.13	0.031	0.65	N	0.157	0.001	0.043	17.0	0.1	1.4	7.1	3.6E+00	3.9E-01	5.7E-02
125	83.86634	-5.11958	0.65	0.024	0.58	N	0.245	0.002	0.069	19.2	0.1	1.4	7.3	3.3E+00	1.8E-01	2.9E-02
127	83.78911	-5.31285	1.11	0.030	0.62	N	0.288	0.002	0.065	21.2	0.1	1.7	7.4	3.3E+00	2.1E-01	3.2E-02
128	83.75322	-5.27003	0.52	0.027	0.66	N	0.220	0.003	0.056	17.9	0.2	1.7	6.9	2.4E+00	1.5E-01	3.3E-02
129	83.88409	-5.09695	3.30	0.046	0.51	N	0.331	0.002	0.044	18.5	0.1	1.1	7.2	2.7E+00	3.5E-01	6.8E-02
130	83.87380	-4.97238	1.74	0.034	0.54	N	0.417	0.002	0.126	19.4	0.1	2.5	7.0	9.0E-01	1.8E-01	1.1E-01
133	84.15429	-6.25039	0.83	0.019	0.53	N	0.288	0.017	0.123	15.5	1.9	3.0	6.9	5.5E-01	2.8E-01	3.4E-01
134	83.80037	-5.57433	0.90	0.024	0.55	N	0.187	0.001	0.046	18.0	0.1	0.9	7.0	1.7E+00	3.4E-01	1.1E-01
137	83.86283	-5.19270	0.74	0.030	0.64	N	0.202	0.001	0.045	19.7	0.0	0.5	7.2	5.6E+00	2.0E-01	1.8E-02
139	83.84413	-5.11082	0.61	0.028	0.67	N	0.391	0.002	0.042	19.3	0.1	1.2	7.3	2.8E+00	8.4E-02	1.5E-02
142	83.88501	-5.10955	0.45	0.018	0.61	N	0.313	0.002	0.056	18.1	0.1	0.9	7.2	1.2E+00	1.4E-01	6.0E-02
144	83.83382	-5.08503	1.75	0.027	0.49	N	0.448	0.003	0.109	19.4	0.1	1.0	7.2	7.9E-01	2.0E-01	1.4E-01
147	83.82629	-5.20081	0.31	0.017	0.65	N	0.232	0.001	0.041	18.0	0.1	1.3	7.2	2.1E+00	1.3E-01	3.4E-02
153	83.78853	-5.86895	1.75	0.031	0.57	N	0.194	0.001	0.061	13.7	0.1	0.8	6.9	1.8E+00	5.9E-01	2.0E-01

Table 1 continued on next page

Table 1 *(continued)*

ID[a]	R.A.[a]	Decl.[a]	M[a]	R_{eff}[a]	C[a]	Pr?[a]	σ_{obs} (km/s)[b]			T_{kin}(K)[b]			$\log(P_c/k_B)$[c]	Vir.[d]	$-\Omega_G/\Omega_K$[d]	$\Omega_G/\Omega_{P,c}$[d]
	(J2000)	(J2000)	($M_\odot$)	(pc)			mn	err	std	mn	err	std	log(K/cm^3)	Rat.		
154	83.73949	-5.76451	1.02	0.017	0.52	N	0.545	0.002	0.076	15.8	0.1	0.8	7.1	2.3E-01	1.4E-01	4.4E-01
161	83.87602	-5.10059	0.72	0.020	0.56	N	0.280	0.002	0.057	18.5	0.1	0.9	7.2	1.3E+00	2.2E-01	8.8E-02
164	83.75679	-5.25595	1.10	0.025	0.50	N	0.317	0.005	0.139	17.4	0.3	2.0	6.9	7.1E-01	2.3E-01	2.0E-01
165	83.68338	-5.69030	1.20	0.017	0.41	Y	0.341	0.007	0.127	13.5	0.5	1.5	7.0	4.1E-01	3.6E-01	7.6E-01
166	83.86629	-5.06040	0.61	0.017	0.57	Y	0.271	0.002	0.088	16.7	0.1	1.0	7.3	1.2E+00	2.3E-01	1.1E-01
167	83.86085	-5.06032	1.95	0.029	0.54	N	0.247	0.001	0.083	16.4	0.1	0.8	7.3	2.1E+00	4.9E-01	1.3E-01
169	83.76035	-5.41373	0.66	0.025	0.54	N	0.663	0.012	0.121	23.4	0.5	1.8	7.3	7.1E-01	4.3E-02	3.1E-02
170	83.82585	-5.22697	0.31	0.017	0.62	N	0.237	0.001	0.044	19.6	0.1	1.4	7.2	1.8E+00	1.3E-01	3.6E-02
172	83.78475	-5.85627	1.78	0.032	0.56	N	0.181	0.001	0.015	14.0	0.2	0.9	6.9	2.0E+00	6.0E-01	1.8E-01
174	83.76215	-5.60311	1.68	0.030	0.51	N	0.160	0.001	0.061	16.2	0.1	0.9	7.1	2.6E+00	6.1E-01	1.3E-01
177	83.85584	-5.09951	0.67	0.019	0.61	N	0.236	0.001	0.046	17.6	0.0	1.0	7.3	1.7E+00	2.6E-01	8.3E-02
179	83.85463	-5.25948	0.27	0.017	0.65	N	0.270	0.010	0.122	21.3	0.8	2.3	7.1	1.6E+00	9.3E-02	3.0E-02
180	83.82183	-5.07955	0.54	0.025	0.49	N	0.785	0.011	0.127	22.5	0.4	2.6	7.2	6.0E-01	2.5E-02	2.1E-02
181	83.89253	-4.99704	0.61	0.021	0.43	Y	0.220	0.004	0.055	19.4	0.3	2.3	7.0	1.5E+00	2.2E-01	8.0E-02
182	83.77374	-4.90811	2.41	0.061	0.55	N	0.223	0.001	0.051	18.8	0.1	1.4	6.8	5.4E+00	3.0E-01	2.9E-02
189	83.72439	-5.77180	2.04	0.033	0.50	N	0.608	0.002	0.170	16.0	0.1	0.8	7.1	5.5E-01	1.2E-01	1.2E-01
191	83.75644	-5.30353	0.31	0.017	0.60	N	0.256	0.008	0.119	16.3	0.5	1.5	7.1	1.6E+00	1.3E-01	4.0E-02
192	83.86733	-5.08365	0.55	0.025	0.68	Y	0.197	0.000	0.010	16.4	0.0	0.5	7.3	5.1E+00	2.0E-01	2.0E-02
193	83.82760	-5.23540	0.63	0.028	0.52	N	0.203	0.001	0.030	21.1	0.1	0.9	7.2	4.0E+00	1.8E-01	2.2E-02
194	83.79358	-5.92738	1.51	0.021	0.50	N	0.254	0.001	0.041	14.3	0.1	0.6	7.0	8.3E-01	5.3E-01	4.7E-01
197	83.87226	-5.20200	1.25	0.047	0.55	N	0.220	0.001	0.069	19.8	0.1	1.1	7.2	9.8E+00	2.0E-01	1.0E-02
198	83.77046	-4.95716	1.52	0.050	0.50	N	0.228	0.002	0.057	18.3	0.2	2.1	7.0	6.6E+00	2.3E-01	1.8E-02
199	83.80018	-5.95131	1.49	0.034	0.63	N	0.221	0.001	0.070	14.1	0.1	1.2	7.1	3.1E+00	3.9E-01	6.6E-02
203	83.82688	-5.08047	0.58	0.027	0.58	N	0.644	0.007	0.168	20.7	0.2	1.9	7.2	9.9E-01	3.7E-02	1.9E-02
207	83.76871	-4.92399	0.42	0.028	0.64	N	0.216	0.001	0.052	18.3	0.1	1.3	6.9	3.6E+00	1.2E-01	1.7E-02

Table 1 continued on next page

Table 1 *(continued)*

ID[a]	R.A.[a]	Decl.[a]	M[a]	R_{eff}[a]	C[a]	Pr?[a]	σ_{obs} (km/s)[b]			T_{kin}(K)[b]			$\log(P_c/k_B)$[c]	Vir.[d]	$-\Omega_G/\Omega_K$[d]	$\Omega_G/\Omega_{P,c}$[d]
	(J2000)	(J2000)	($M_\odot$)	(pc)			mn	err	std	mn	err	std	log(K/cm^3)	Rat.		
208	83.78403	-4.93252	0.32	0.022	0.65	N	0.233	0.002	0.055	18.3	0.1	1.6	6.9	2.4E+00	1.1E-01	2.3E-02
211	83.72458	-4.95249	0.98	0.028	0.52	N	0.259	0.004	0.060	16.7	0.2	1.1	6.8	1.1E+00	2.4E-01	1.3E-01
213	83.92177	-5.04128	0.94	0.021	0.46	N	0.184	0.005	0.041	14.8	0.4	1.5	6.9	1.1E+00	4.5E-01	2.7E-01
220	83.75208	-5.66773	0.73	0.030	0.51	N	0.293	0.005	0.212	17.6	0.3	2.0	7.1	2.7E+00	1.4E-01	2.7E-02
221	83.73876	-5.34577	0.72	0.028	0.52	N	0.551	0.008	0.135	20.5	0.4	1.4	7.1	9.8E-01	5.6E-02	2.9E-02
223	83.75273	-4.97396	0.28	0.021	0.68	N	0.284	0.004	0.078	16.8	0.3	1.7	6.9	1.9E+00	8.1E-02	2.2E-02
225	83.78123	-5.94482	0.88	0.026	0.62	N	0.171	0.001	0.064	13.0	0.1	1.2	7.0	3.1E+00	4.0E-01	6.7E-02
226	83.76019	-5.63125	0.69	0.025	0.60	N	0.227	0.001	0.048	14.9	0.1	0.7	7.1	2.6E+00	2.3E-01	4.7E-02
228	83.75243	-5.36597	0.56	0.021	0.51	N	0.464	0.005	0.200	22.1	0.2	1.6	7.3	1.1E+00	7.5E-02	3.6E-02
231	83.79408	-4.99982	1.21	0.039	0.55	N	0.422	0.003	0.117	19.1	0.2	1.7	7.1	2.5E+00	1.1E-01	2.1E-02
232	83.82275	-4.94168	0.32	0.023	0.53	N	0.446	0.007	0.086	23.3	0.4	3.7	7.0	1.1E+00	4.2E-02	1.9E-02
234	83.78691	-5.88847	0.81	0.021	0.55	N	0.184	0.003	0.061	13.9	0.2	1.1	7.0	1.3E+00	4.2E-01	1.9E-01
235	83.74957	-5.33127	0.29	0.017	0.65	N	0.426	0.014	0.145	16.4	0.9	4.4	7.2	1.0E+00	5.9E-02	2.9E-02
239	83.75886	-5.29740	0.34	0.019	0.62	N	0.228	0.005	0.099	16.3	0.4	1.5	7.1	2.1E+00	1.5E-01	3.5E-02
240	83.71620	-4.93830	0.26	0.017	0.57	N	0.223	0.007	0.083	18.1	0.6	2.2	6.8	1.0E+00	1.2E-01	6.1E-02
241	83.77792	-4.93596	0.46	0.017	0.56	N	0.232	0.001	0.045	17.9	0.1	1.0	7.0	8.9E-01	2.0E-01	1.3E-01
245	83.82808	-5.06771	0.22	0.027	0.71	N	0.647	0.006	0.118	21.8	0.3	1.6	7.2	2.6E+00	1.4E-02	2.6E-03
246	83.87723	-5.87634	1.10	0.019	0.52	N	0.194	0.002	0.065	12.0	0.3	1.0	6.8	8.2E-01	6.3E-01	6.2E-01
247	83.81210	-5.27932	0.49	0.020	0.45	N	0.328	0.008	0.123	25.2	0.6	1.4	7.3	1.5E+00	1.1E-01	3.8E-02
249	83.84900	-5.09092	0.30	0.017	0.66	N	0.229	0.001	0.052	16.9	0.1	1.0	7.3	2.8E+00	1.4E-01	2.5E-02
250	83.87190	-4.99081	1.65	0.053	0.60	N	0.439	0.003	0.188	18.5	0.1	1.4	7.1	4.2E+00	1.0E-01	1.2E-02
254	83.90602	-6.16198	0.45	0.017	0.60	N	0.195	0.006	0.095	14.4	0.8	4.0	6.9	1.0E+00	2.6E-01	1.5E-01
256	83.79314	-5.27891	0.46	0.021	0.47	N	0.507	0.015	0.164	21.8	0.8	4.3	7.2	8.9E-01	5.5E-02	3.2E-02
257	83.75793	-5.23305	0.44	0.019	0.54	N	0.572	0.014	0.134	15.7	1.0	2.8	6.8	2.4E-01	5.0E-02	1.1E-01
259	83.74219	-5.33073	0.29	0.022	0.64	N	0.439	0.015	0.134	16.0	0.9	3.0	7.1	1.5E+00	4.5E-02	1.5E-02

Table 1 continued on next page

Table 1 *(continued)*

ID[a]	R.A.[a]	Decl.[a]	M[a]	R_{eff}[a]	C[a]	Pr?[a]	σ_{obs} (km/s)[b]			T_{kin}(K)[b]			$\log(P_c/k_B)$[c]	Vir.[d]	$-\Omega_G/\Omega_K$[d]	$\Omega_G/\Omega_{P,c}$[d]
	(J2000)	(J2000)	($M_\odot$)	(pc)			mn	err	std	mn	err	std	log(K/cm^3)	Rat.		
260	83.81226	-5.26960	0.67	0.027	0.50	N	0.285	0.004	0.059	21.2	0.2	2.9	7.2	3.0E+00	1.4E-01	2.3E-02
264	83.75742	-5.92680	4.16	0.052	0.49	N	0.258	0.001	0.061	13.5	0.1	0.6	7.0	2.9E+00	6.1E-01	1.2E-01
265	84.10731	-6.23729	0.94	0.025	0.54	N	0.440	0.002	0.046	12.8	0.1	0.7	6.9	5.8E-01	1.3E-01	1.3E-01
266	83.91805	-5.11422	0.32	0.017	0.48	N	0.315	0.008	0.132	19.2	0.5	2.4	7.0	9.3E-01	9.5E-02	5.4E-02
269	83.83881	-5.17787	0.71	0.028	0.53	N	0.180	0.001	0.030	18.7	0.1	0.9	7.2	5.2E+00	2.3E-01	2.3E-02
274	83.70746	-5.77024	0.59	0.032	0.57	N	0.479	0.002	0.180	16.3	0.1	0.9	7.1	2.4E+00	5.3E-02	1.1E-02
282	84.09522	-6.21789	0.39	0.017	0.57	N	0.297	0.002	0.127	13.9	0.1	0.6	6.9	8.1E-01	1.4E-01	9.5E-02
283	83.85865	-5.87194	1.11	0.028	0.54	N	0.274	0.002	0.080	12.0	0.2	0.9	6.9	1.2E+00	2.9E-01	1.4E-01
287	83.66783	-5.52075	0.89	0.034	0.59	N	0.260	0.005	0.081	14.2	0.6	1.5	6.7	2.0E+00	1.9E-01	5.1E-02
291	83.77259	-5.30811	0.18	0.018	0.62	N	0.157	0.004	0.056	17.9	0.5	2.0	7.3	6.0E+00	1.1E-01	8.9E-03
292	83.88603	-5.15899	0.27	0.022	0.48	N	0.230	0.004	0.062	22.5	0.3	2.3	7.2	4.4E+00	8.4E-02	9.6E-03
293	83.90896	-5.01580	0.40	0.031	0.66	N	0.200	0.006	0.035	15.5	0.6	1.6	6.9	6.1E+00	1.2E-01	1.0E-02
294	84.10313	-6.23431	3.60	0.051	0.45	N	0.448	0.002	0.046	12.9	0.1	0.8	6.9	1.2E+00	2.4E-01	1.1E-01
300	83.88596	-5.16940	0.29	0.017	0.44	N	0.246	0.003	0.058	22.0	0.2	2.0	7.2	1.9E+00	1.1E-01	2.8E-02
302	83.82228	-5.04308	0.56	0.035	0.59	N	0.491	0.006	0.114	22.7	0.3	3.1	7.2	3.7E+00	4.2E-02	5.7E-03
306	83.77675	-5.28182	0.31	0.032	0.59	N	0.279	0.011	0.117	21.7	1.1	4.3	7.1	8.1E+00	5.5E-02	3.4E-03
310	83.76282	-5.46122	0.17	0.020	0.58	N	1.007	0.032	0.087	29.3	1.5	7.1	7.0	3.8E-01	6.4E-03	8.5E-03
312	83.71450	-5.64783	0.80	0.036	0.49	N	0.455	0.008	0.110	17.8	0.5	1.4	7.0	2.0E+00	6.8E-02	1.8E-02
317	83.75261	-5.32364	0.59	0.022	0.46	N	0.432	0.017	0.109	15.9	1.1	3.0	7.2	1.1E+00	9.1E-02	4.5E-02
319	83.70721	-4.91835	0.28	0.026	0.62	N	0.207	0.009	0.005	21.4	0.8	0.4	6.7	2.6E+00	8.2E-02	1.6E-02
323	83.81324	-5.28590	0.21	0.024	0.63	N	0.721	0.017	0.083	25.0	0.7	1.7	7.3	1.9E+00	1.2E-02	3.1E-03
327	83.87514	-5.08087	0.41	0.026	0.63	N	0.204	0.001	0.019	16.4	0.1	0.8	7.2	7.1E+00	1.4E-01	1.0E-02
330	83.81624	-5.25487	1.71	0.058	0.53	N	0.311	0.002	0.046	20.3	0.1	1.2	7.2	8.8E+00	1.5E-01	8.7E-03
331	83.82015	-5.24576	0.25	0.017	0.53	N	0.224	0.002	0.074	21.0	0.2	1.4	7.1	2.2E+00	1.0E-01	2.4E-02
342	83.79221	-5.63126	1.75	0.052	0.48	N	0.567	0.006	0.124	16.9	0.3	2.0	7.0	2.0E+00	7.3E-02	1.9E-02

Table 1 continued on next page

Table 1 *(continued)*

ID[a]	R.A.[a]	Decl.[a]	M[a]	R_{eff}[a]	C[a]	Pr?[a]	σ_{obs} (km/s)[b]			T_{kin}(K)[b]			$\log(P_c/k_B)$[c]	Vir.[d]	$-\Omega_G/\Omega_K$[d]	$\Omega_G/\Omega_{P,c}$[d]
	(J2000)	(J2000)	($M_\odot$)	(pc)			mn	err	std	mn	err	std	log(K/cm^3)	Rat.		
353	83.73182	-5.33475	0.10	0.026	0.74	N	0.566	0.030	0.148	22.3	2.3	6.0	7.0	4.3E+00	7.9E-03	9.1E-04
355	83.91499	-5.10713	1.54	0.079	0.57	N	0.334	0.005	0.111	20.7	0.3	3.2	7.0	1.7E+01	9.1E-02	2.7E-03
357	84.08591	-6.22051	0.32	0.020	0.65	N	0.321	0.003	0.111	13.9	0.1	0.6	6.9	1.3E+00	8.9E-02	3.5E-02
361	83.68854	-5.73855	0.73	0.025	0.52	N	0.154	0.001	0.052	12.7	0.1	1.4	7.1	4.0E+00	3.8E-01	5.0E-02
362	83.75024	-5.64903	0.72	0.035	0.60	N	0.207	0.002	0.069	15.5	0.1	1.3	7.1	6.9E+00	1.9E-01	1.4E-02
363	83.72537	-5.62012	0.32	0.033	0.59	N	0.402	0.006	0.122	22.0	2.0	6.0	7.0	4.5E+00	3.4E-02	3.8E-03
367	83.82254	-5.18514	0.14	0.025	0.71	N	0.167	0.004	0.070	20.0	0.5	3.5	7.2	1.8E+01	5.1E-02	1.4E-03
371	83.73876	-5.69251	1.48	0.044	0.44	N	0.227	0.002	0.175	15.0	0.1	1.8	7.1	6.2E+00	2.8E-01	2.4E-02
387	83.70517	-5.69387	0.19	0.020	0.59	Y	0.842	0.016	0.148	17.0	0.7	1.8	7.1	5.7E-01	1.0E-02	8.8E-03
390	83.89300	-5.08923	0.12	0.021	0.68	N	0.466	0.012	0.149	22.2	0.7	2.3	7.2	3.5E+00	1.6E-02	2.4E-03
391	83.79428	-4.97123	0.11	0.021	0.65	N	0.446	0.005	0.082	21.6	0.2	3.3	7.1	3.5E+00	1.6E-02	2.2E-03
401	83.76262	-4.98428	0.34	0.026	0.60	N	0.274	0.004	0.092	16.6	0.3	2.1	7.0	3.3E+00	8.4E-02	1.3E-02
402	83.71703	-4.94449	0.47	0.034	0.55	N	0.235	0.004	0.056	16.7	0.3	1.3	6.8	3.9E+00	1.1E-01	1.4E-02
405	83.74210	-5.70125	1.13	0.051	0.55	N	0.201	0.002	0.123	15.1	0.1	1.7	7.1	1.5E+01	2.1E-01	7.1E-03
407	83.75100	-5.41395	0.85	0.070	0.61	N	0.662	0.011	0.162	23.7	0.6	4.3	7.2	1.0E+01	1.9E-02	9.4E-04
413	83.73518	-5.56496	0.76	0.022	0.43	N	0.160	0.002	0.043	13.3	0.3	1.5	6.9	1.8E+00	4.2E-01	1.3E-01
420	83.74128	-5.72616	0.17	0.026	0.67	N	0.225	0.002	0.104	15.5	0.1	1.2	7.1	1.2E+01	5.3E-02	2.2E-03
422	83.89687	-5.17238	0.29	0.038	0.57	N	0.204	0.004	0.062	20.9	0.3	2.2	7.1	2.0E+01	6.0E-02	1.5E-03
431	83.75942	-5.63871	0.49	0.030	0.63	N	0.216	0.001	0.049	14.8	0.1	0.8	7.1	6.5E+00	1.4E-01	1.1E-02
432	83.79646	-5.62771	0.45	0.020	0.48	N	0.522	0.007	0.100	16.0	0.4	1.8	7.0	5.1E-01	5.6E-02	5.8E-02
434	83.73855	-4.95586	0.18	0.021	0.58	N	0.290	0.009	0.094	17.7	0.7	1.9	6.9	2.3E+00	5.1E-02	1.1E-02
440	83.78488	-5.96492	0.86	0.042	0.61	N	0.183	0.001	0.044	13.9	0.1	0.7	7.0	1.1E+01	2.2E-01	1.0E-02
441	83.71771	-5.73641	0.81	0.045	0.54	N	0.931	0.007	0.094	15.0	0.2	2.5	7.1	1.5E+00	1.6E-02	5.3E-03
461	83.80562	-5.16646	0.22	0.018	0.47	N	0.470	0.017	0.139	21.1	1.1	4.3	7.1	9.7E-01	3.5E-02	1.8E-02
462	83.90534	-5.10844	0.44	0.053	0.64	N	0.372	0.006	0.162	20.6	0.3	3.5	7.1	1.9E+01	3.3E-02	9.0E-04

Table 1 continued on next page

Table 1 *(continued)*

ID[a]	R.A.[a]	Decl.[a]	M[a]	R_{eff}[a]	C[a]	Pr?[a]	σ_{obs} (km/s)[b]			T_{kin}(K)[b]			$\log(P_c/k_B)$[c]	Vir.[d]	$-\Omega_G/\Omega_K$[d]	$\Omega_G/\Omega_{P,c}$[d]
	(J2000)	(J2000)	($M_\odot$)	(pc)			mn	err	std	mn	err	std	log(K/cm^3)	Rat.		
463	83.87745	-5.04815	0.28	0.036	0.56	N	0.483	0.016	0.152	20.0	0.9	3.4	7.2	8.3E+00	2.1E-02	1.3E-03
464	83.77074	-4.94613	0.40	0.031	0.56	N	0.219	0.001	0.044	17.5	0.1	0.8	7.0	5.8E+00	1.0E-01	9.1E-03
469	83.80346	-5.92901	0.33	0.024	0.59	N	0.238	0.001	0.037	14.4	0.1	0.7	7.0	4.1E+00	1.1E-01	1.4E-02
470	83.74294	-5.68198	0.68	0.051	0.54	N	0.825	0.008	0.124	17.0	0.2	2.8	7.1	2.7E+00	1.5E-02	2.7E-03
471	83.81435	-5.55115	0.88	0.058	0.55	N	0.785	0.024	0.095	19.3	1.0	3.7	6.9	2.1E+00	1.8E-02	4.4E-03
478	83.82794	-5.93413	0.60	0.035	0.60	N	0.170	0.002	0.050	12.7	0.9	2.0	7.0	9.2E+00	2.1E-01	1.1E-02
486	83.92940	-5.09902	0.16	0.037	0.64	N	0.597	0.028	0.104	28.2	1.9	4.6	6.9	4.8E+00	8.0E-03	8.3E-04
493	84.15930	-6.26998	0.14	0.027	0.63	N	0.443	0.057	0.037	20.2	4.4	0.0	6.9	3.6E+00	1.7E-02	2.3E-03
498	83.77784	-5.26313	0.52	0.059	0.65	N	0.355	0.018	0.214	18.4	1.4	5.6	7.0	1.9E+01	4.0E-02	1.0E-03
500	83.90644	-5.09942	0.36	0.030	0.49	N	0.344	0.006	0.103	21.0	0.3	2.6	7.1	4.3E+00	5.4E-02	6.4E-03
508	83.88870	-6.10200	0.10	0.017	0.65	Y	0.774	0.019	0.145	17.6	1.9	1.9	6.9	5.6E-01	7.2E-03	6.5E-03
518	83.89446	-5.18567	0.09	0.027	0.67	N	0.275	0.016	0.081	23.2	1.4	1.9	7.1	1.8E+01	1.8E-02	5.2E-04
524	83.75788	-5.88522	0.26	0.034	0.62	N	0.767	0.017	0.219	15.7	0.9	3.7	7.0	1.9E+00	9.7E-03	2.6E-03
535	83.92459	-6.12882	0.56	0.048	0.58	N	0.248	0.003	0.198	13.6	0.3	1.2	6.9	1.3E+01	9.3E-02	3.5E-03
537	83.78815	-5.91879	0.35	0.033	0.68	N	0.254	0.001	0.039	14.1	0.1	0.6	7.0	8.6E+00	8.0E-02	4.7E-03
538	83.71536	-5.70617	0.29	0.031	0.61	N	0.734	0.007	0.199	16.9	0.2	2.2	7.1	2.0E+00	1.3E-02	3.2E-03
539	83.95736	-5.51178	0.28	0.034	0.65	N	0.854	0.064	0.127	20.5	2.3	6.1	6.5	4.6E-01	8.5E-03	9.4E-03
540	83.72819	-5.40841	0.17	0.030	0.63	N	0.798	0.016	0.197	22.5	0.7	2.4	7.0	1.8E+00	6.5E-03	1.8E-03
543	83.87811	-5.12074	0.29	0.035	0.50	N	0.212	0.002	0.046	18.4	0.2	1.9	7.3	2.2E+01	6.7E-02	1.5E-03
545	83.76186	-4.93142	0.18	0.026	0.61	N	0.262	0.002	0.074	18.0	0.1	1.1	6.9	6.0E+00	4.5E-02	3.7E-03
546	83.73587	-4.90142	0.10	0.022	0.69	N	0.162	0.004	0.019	18.4	0.4	1.8	6.8	6.2E+00	4.6E-02	3.7E-03
551	83.88134	-5.89270	1.13	0.050	0.56	N	0.168	0.001	0.066	11.3	0.1	0.9	6.8	1.1E+01	2.9E-01	1.4E-02
554	83.75212	-5.30263	0.68	0.046	0.54	N	0.281	0.007	0.108	16.0	0.4	1.5	7.0	1.1E+01	9.4E-02	4.4E-03
570	84.16045	-6.26304	0.45	0.033	0.55	N	0.304	0.046	0.032	12.6	3.1	1.6	6.9	4.0E+00	8.6E-02	1.1E-02
571	84.01832	-6.16034	0.22	0.036	0.56	N	0.473	0.007	0.114	17.8	0.4	1.5	6.8	4.3E+00	1.8E-02	2.1E-03

Table 1 continued on next page

Table 1 *(continued)*

ID[a]	R.A.[a]	Decl.[a]	M[a]	R_{eff}[a]	C[a]	Pr?[a]	σ_{obs} (km/s)[b]			T_{kin}(K)[b]			$\log(P_c/k_B)$[c]	Vir.[d]	$-\Omega_G/\Omega_K$[d]	$\Omega_G/\Omega_{P,c}$[d]
	(J2000)	(J2000)	($M_\odot$)	(pc)			mn	err	std	mn	err	std	log(K/cm^3)	Rat.		
572	83.72882	-5.72719	1.79	0.089	0.60	N	0.299	0.002	0.199	15.4	0.1	1.4	7.1	3.3E+01	1.2E-01	1.8E-03
584	83.85491	-5.98366	0.31	0.020	0.45	N	0.186	0.004	0.115	15.5	0.5	1.4	7.0	2.7E+00	1.5E-01	2.9E-02
586	83.67780	-5.47204	0.58	0.041	0.47	N	0.294	0.008	0.139	17.0	0.9	3.6	6.7	3.7E+00	8.2E-02	1.1E-02
588	83.92395	-5.08629	0.10	0.028	0.60	N	0.185	0.037	0.111	24.6	5.5	0.0	6.9	1.5E+01	2.7E-02	8.9E-04
592	83.86800	-5.99738	0.55	0.043	0.57	N	0.237	0.002	0.051	14.0	0.1	1.1	6.9	1.1E+01	1.0E-01	4.7E-03
594	83.70678	-5.74392	0.37	0.024	0.42	N	0.549	0.006	0.169	17.9	0.2	1.1	7.1	1.2E+00	3.5E-02	1.5E-02
595	83.69590	-5.70022	0.39	0.040	0.55	Y	0.718	0.010	0.154	16.6	0.4	1.7	7.1	3.0E+00	1.4E-02	2.3E-03
601	83.64971	-5.68440	0.25	0.023	0.60	N	0.270	0.023	0.266	13.5	4.1	0.0	6.9	2.7E+00	7.8E-02	1.5E-02
603	83.87687	-5.06588	0.49	0.037	0.60	N	0.216	0.003	0.069	16.9	0.3	2.3	7.2	1.6E+01	1.1E-01	3.4E-03
610	84.12174	-6.25239	0.81	0.041	0.49	N	0.357	0.003	0.042	13.9	0.2	1.8	6.9	3.6E+00	9.5E-02	1.3E-02
611	83.82141	-5.99614	0.43	0.049	0.62	N	0.155	0.002	0.109	14.0	0.2	1.2	7.0	3.9E+01	1.1E-01	1.4E-03
612	83.68629	-5.78575	1.56	0.130	0.64	N	0.606	0.003	0.102	15.9	0.1	1.6	7.0	3.3E+01	2.3E-02	3.6E-04
616	83.87311	-5.05444	0.26	0.031	0.56	N	0.255	0.003	0.066	17.2	0.2	1.4	7.2	1.5E+01	5.8E-02	2.0E-03
622	83.76991	-5.92961	0.40	0.026	0.52	N	0.217	0.002	0.069	13.5	0.1	1.0	7.0	4.8E+00	1.4E-01	1.5E-02
623	83.71152	-5.71424	0.86	0.061	0.52	N	0.659	0.005	0.146	16.5	0.2	1.8	7.1	6.2E+00	2.3E-02	1.9E-03
630	83.81553	-5.05844	0.13	0.034	0.66	N	0.525	0.005	0.056	23.0	0.8	2.1	7.2	1.1E+01	9.1E-03	4.1E-04
632	83.93491	-6.13118	0.58	0.045	0.59	N	0.252	0.003	0.202	14.0	0.2	1.5	6.9	1.0E+01	9.9E-02	4.8E-03
637	83.80293	-5.21256	0.12	0.034	0.64	N	0.725	0.052	0.128	24.9	2.3	4.3	7.1	5.5E+00	4.7E-03	4.2E-04
648	83.80923	-5.17569	0.19	0.027	0.53	N	0.446	0.019	0.076	22.0	1.3	3.6	7.1	4.1E+00	2.2E-02	2.6E-03
686	83.73658	-5.80658	0.22	0.036	0.57	N	0.782	0.011	0.149	16.3	0.7	2.3	7.0	2.7E+00	7.6E-03	1.4E-03
691	83.75529	-5.46870	0.26	0.033	0.63	N	1.111	0.073	0.079	15.7	4.0	0.0	6.9	8.2E-01	4.9E-03	3.0E-03
699	83.75322	-4.89717	0.48	0.067	0.59	N	0.146	0.005	0.035	17.6	0.8	3.0	6.8	4.2E+01	7.8E-02	9.3E-04
701	83.75135	-5.89591	0.58	0.065	0.59	N	0.738	0.010	0.112	15.9	0.5	3.5	7.0	6.2E+00	1.2E-02	9.7E-04
702	83.72680	-4.96436	0.21	0.030	0.58	N	0.302	0.008	0.118	17.2	0.5	1.5	6.8	4.4E+00	4.0E-02	4.6E-03
707	83.75019	-5.81241	0.47	0.064	0.61	N	0.619	0.007	0.115	16.9	0.4	2.7	7.0	1.1E+01	1.4E-02	6.3E-04

Table 1 continued on next page

Table 1 *(continued)*

ID[a]	R.A.[a]	Decl.[a]	M[a]	R_{eff}[a]	C[a]	Pr?[a]	σ_{obs} (km/s)[b]			T_{kin}(K)[b]			$\log(P_c/k_B)$[c]	Vir.[d]	$-\Omega_G/\Omega_K$[d]	$\Omega_G/\Omega_{P,c}$[d]
	(J2000)	(J2000)	($M_\odot$)	(pc)			mn	err	std	mn	err	std	$\log(K/cm^3)$	Rat.		
721	83.67246	-5.69374	0.32	0.042	0.66	N	0.248	0.006	0.126	13.3	0.7	2.2	7.0	1.8E+01	6.1E-02	1.7E-03
734	83.74316	-5.83421	0.55	0.072	0.62	N	0.688	0.010	0.148	17.1	0.6	2.0	7.0	9.8E+00	1.2E-02	6.1E-04
750	83.82236	-5.58375	0.21	0.047	0.63	N	0.793	0.065	0.071	23.0	2.5	6.7	6.9	4.7E+00	5.2E-03	5.5E-04
755	83.73468	-5.90930	0.37	0.069	0.67	N	0.649	0.009	0.092	16.1	0.4	3.0	6.9	1.3E+01	9.2E-03	3.6E-04
768	83.78508	-6.00744	0.56	0.063	0.66	N	0.248	0.006	0.118	14.2	0.7	1.9	7.0	3.5E+01	6.9E-02	9.8E-04
784	84.01330	-6.23102	0.13	0.034	0.64	N	0.562	0.007	0.050	17.4	0.4	2.1	6.8	5.0E+00	8.3E-03	8.4E-04
790	83.80356	-4.93682	0.43	0.108	0.59	N	0.464	0.011	0.128	27.4	0.8	5.2	7.0	7.5E+01	1.1E-02	7.3E-05
816	83.73568	-5.36760	0.10	0.030	0.72	N	0.624	0.011	0.111	22.0	0.5	1.9	7.1	6.4E+00	6.0E-03	4.7E-04
835	83.65690	-5.69668	0.45	0.036	0.57	N	0.277	0.012	0.184	13.2	2.2	0.2	6.9	6.4E+00	8.7E-02	6.9E-03
869	83.80022	-5.78781	0.16	0.061	0.60	N	0.374	0.032	0.059	26.4	5.9	0.0	6.7	2.7E+01	9.6E-03	1.8E-04
871	83.72573	-5.80079	0.40	0.064	0.61	N	0.881	0.011	0.114	16.6	0.4	1.4	7.1	7.5E+00	6.2E-03	4.1E-04
873	83.86276	-4.95504	0.67	0.057	0.53	N	0.396	0.007	0.090	27.5	0.4	2.8	6.9	8.5E+00	4.0E-02	2.3E-03
879	83.80411	-6.02245	0.42	0.085	0.72	N	0.930	0.053	0.072	15.8	2.8	0.0	7.0	1.3E+01	4.4E-03	1.7E-04
907	83.84457	-6.05341	0.95	0.096	0.66	N	0.597	0.007	0.126	15.2	0.4	2.4	6.9	1.7E+01	2.0E-02	5.9E-04

[a]Core properties based on the *getsources* catalogue of Lane et al. (2016). Only cores which have kinematic properties measured by GAS are listed. Columns are the core ID in Lane et al. (2016), central position, mass (estimated using eqn 1 from the total flux), effective radius (geometric mean of the major and minor axis lengths), concentration as derived using equation 11 and whether the core has an associated protostar. [b]Velocity dispersion (σ_{obs}) and kinetic temperature (T_{kin}) measured for the cores, averaging over all core pixels where sufficient signal was present. The value reported for each quantity is the mean weighted by the inverse square of the uncertainty. The formal error in the weighted mean value is also reported (second column), as is the weighted standard deviation (third column). This latter quantity is more reflective of the variation between fitted values across the core. [c]Estimated pressure on the core boundary due to the weight of the overlying cloud material. See Section 3.2 for more information. [d]Virial parameters estimated according to Section 3.2. The virial ratio is given by $-(\Omega_G+\Omega_{P,c})/2\Omega_K$. $-\Omega_G/\Omega_K$ reflects the balance of gravitational binding versus thermal pressure, while $\Omega_G/\Omega_{P,c}$ reflects whether gravity or external cloud pressure dominates the confinement of the cores.